Transient Absorption Spectroscopy of Poly(3-hexylthiophene):PCBM Solar Cells

AALBORG UNIVERSITY
STUDENT REPORT

Andreas Valentin Pedersen

April 10, 2018

Department of Materials and Production.
Aalborg University

Department of Materials & Production
Skjernvej 4A
9220 Aalborg Ø
Telephone (+45) 9940 9215
http://www.nano.aau.dk

Title:
Transient Absorption Spectroscopy of Poly(3-hexylthiophene):PCBM Solar Cells

Project period:
1nd September 2017 to
10th April 2018

Author:

Andreas Valentin Pedersen

Supervisor:
Esben Skovsen

No. of Pages: 47

No. of Appendix Pages: 8

Total no. of pages: 61

Completed: 10-04-18

Abstract:

This project investigates the dynamics of excited states in polymeric organic solar cells through transient absorption spectroscopy. The conjugated polymer poly(3-hexylthiophene-2,5-diyl)(P3HT) is studied in the role as electron donor paired with the fullerene derivative [6,6]-phenyl-C_{71}-butyric acid methyl ester (PCBM) as electron acceptor. Via a set-up build as a part of the project, the transient absorption of P3HT and P3HT:PCBM as function of pump-probe delay is measured at selected wavelengths ranging from 650 nm to 1200 nm. The lifetime of the transient absorption is evaluated by biexponential fits. The result is a fast term decaying with lifetime of a few picoseconds and a slowly decaying term with lifetime ranging from tens to hundreds of picoseconds. The decay-times for each measurement are found not to be consistent with each other with regards to the expected transient absorption spectrum. The decays are concluded to be primarily caused by bimolecular recombination of the excited species due to a high pump fluence of $\sim 500\ \mu J \cdot \mathrm{cm}^{-2}$.

Resume

I projektet undersøges rekombination af fotoeksiterede ladningsbærere i organiske halvledende materialer: Polymeren poly(3-hexylthiophene-2,5-diyl)(P3HT) og en 1:1 blanding af P3HT og [6,6]-phenyl-C_{71}-butyric acid methyl ester (PCBM). Eksperimentielt undersøges tre tyndfilmsprøver, nemlig P3HT, annealet P3HT:PCBM og uberørt P3HT:PCBM. Dog er det uvist hvilken af P3HT:PCBM prøverne der blevet annealet. Dette gøres ved ultrahurtig pumpe-probe absorptionsspektroskopi, hvor et højenergi femtoskeund pumpebeam exciterer grundtilstanden i P3HT makromolekylerne og et lavenergi femtosekund superkontinuum probebeam måler ændringen i absorbance som funktion af tiden når de exciterede tilstande henfalder til grundtilstanden eller lavere eksiterede tilstande.

Fra teoretisk perspektiv introduceres organiske halvledere, deres brug i organiske solceller og de eksiterede tilstande heri. Pga. en høj dielektrisk konstant ift. uorganiske halvledere, formes neutrale excitoner frem for adskilte ladningsbærere ved excitation af en elektron over båndgabet. Singlet versionerne af disse excitoner har en høj bindingsenergi, typisk omkring 0.3 eV, og henfalder derfor radiativt over få nanosekunder hvis ikke bindingsenergien overkommes inden. I tilfældet hvor excitonen splittes i et positivt hul og en negativ fri elektron, deformerer de molekyler der er værter for ladningerne, hvilket giver anledning til tilstande mellem højest besatte molekylære orbital of laveste ubesatte molekylære orbital(LUMO). Konstruktionen af state-of-the-art organiske solceller, er opbygget omkring effektiv omdannelse af excitnoner til polaroner. Hvis LUMO i acceptoren er lavere med excitonens bindingsenergi ift. donorens LUMO, vil elektronen overgå til acceptoren mend hullet bliver tilbage i donoren - ladningerne er blevet adskilt. Eftersom excitonerne blot diffunderer nogle få nanometer før de rekombinerer, er sammenblandingen vigtig for at excitonerne når til en grænsefalde mellem donor og acceptor før de henfalder.

Inden beskrivelse og diskussion af det udførte eksperiment, introduceres også de vigtigste ikke-lineære optiske processer der er styrrende for generationen af superkontinuum puslerne deres bruges som probe. Disse pulser genereres i en safir crystal, hvor safirens 3. orderns ikke-linære succeptibilitet introducerer en intensintetsafhængighed i brydningsindekset. Dette giver et ekstra bidrag til pulsens fase som varierer over tid med ændringen i pulsens intensitet over tid. Dette medfører en ændring i pulsens frekvens proportional med den tidsafledte af fasen.

Ændringen i absorbance over tid ved bølgelængderne 650 nm, 700 nm, 850 nm, 1000 nm, 1100 nm og 1200 nm viser sig gennem pump-probe eksperimentet generelt at følge en dobbelteskponentiel udvikling. Ved at fitte en dobbelteksponentiel funktion til de eksperimentelt målte data for absorbansændringen efter foton-eksitering, kan rekombinationen af singlet excitoner gennem andenordens henfalskanaler estimeres til ske med en levetider i intervallet 1-10 ps.

Preface

This report is written on the 4. semester of the author's masters degree in physics from the Department of Materials and Production at Aalborg University. The extent of the thesis work is 30 ECTS and it was done during the autumn semester of 2017 and half of the spring semester of 2018.

Reading Guide

Succeeding chapters support each other, and it is therefore recommended to read the report chronologically. When referring to equations or the like in the text, *equation* will be shortened Eq., *chapter* will be shortened Ch., and so forth. The external references used in this work appear in numbered order in brackets in the text and are listed in the bibliography at the end of the report in order of succession.

Contents

Chapter 1

Introduction

The semiconducting properties of π-conjugated polymers and small molecules, has led to realization of light emitting diodes[1, 2], field effect transistors [3, 4] and photovoltaic cells [5, 6] with active layers comprised of organic compounds. Research in organic photovoltaic devices, in particular, is ongoing due to the strong motivational factor of harvesting energy directly from the sun and the room for improvement in doing so with organic compounds. This is desirable because of abundant availability of organic semiconducting material due to synthesis possibilities, tunable physical properties, outlook to economically efficient large scale production via. e.g. roll-to-roll techniques, and flexibility of the material [5]. The research is focused on solving the inherent drawbacks of OSCs:

1. Low charge carrier mobility due to disorder in the organic crystals
2. Large binding energy between the electron and the hole of the primary photoexcitations, excitons
3. Poor stability due to light-induced degradation, oxidation and thermal degradation [7]

The carrier mobility can be increased by controlling the structure of the active layer by annealing[8] or the choice of solvent[9] and charge separation effiencies has been brought close to one in the bulk heterojunction (BHJ) devices where the acceptor and the donor is mixed together[10]. Single-cell annealed BHJ devices using polymer donor and fullerene acceptors thus exhibit efficiencies of up to 10%[11] and reproducible efficiencies approaching 5%[12, 13]. As a decent efficiency has now been reached, improving the stability of the OSCs has now become an area of increasing interest. This thesis was indeed initiated with the goal of studying photodegradation in the small molecule organic solar cell (SMOSC) using tetra phenyl dibenzoperiflanthene DBP as a donor and fullerene as acceptor DBP:fullerene. The efficiency of small molecule organic solar cells has been lacking behind polymer solar cells (PCSs), and the stability of SMOSCs is therefore not studied to the same degree as PSCs. The donor DBP in particular, is not very well studied.

Due to limited time, the experimental set-up produced with the intend of studying DBP:fullerene photovoltaics, was instead used to observe dynamics of excited states in the more well studied system comprised of the donor poly(3-hexylthiophene-2,5-diyl) (P3HT) and the acceptor [6,6]-phenyl-C_{71}-butyric acid methyl ester (PCBM). This is done via transient absorption spectroscopy (TAS) on the picosecond time scale, which is a pump-probe technique where the absorbance difference due to photoexcitations in the sample is measured. The set-up produced for conduction of experiments with regards to this thesis uses femtosecond supercontinuum pulses for probing and 520 nm femtosecond pulses for pumping. This allows for analysis of dynamics of excited species which exhibit characteristic lifetimes on the picosecond scale or longer. By varying the delay between the pump pulse and the probe pulse over ~ 1 ns, the decay of singlet excitons can be assessed and the extend to which polarons are produced can be observed. Under the right circumstances, this information can be used to deduce the nano scale structure of the investigated samples and the mobility of excited species.

Chapter 2

Organic Semiconductors

An introduction to organic semiconductors is essential for the understanding of organic solar cells. In this chapter, basic theory of organic semiconductors is presented together with the concepts of excitons and polarons.

Organic semiconductors are crystals comprised of molecular units held together by van der Waals forces. Due to the small strength of the van der Waals forces compared to the intramolecular forces, the conductivity and electronic energy structure is, to a large part, tied up on the individual molecules. The approach to organic semiconductors therefore starts from a molecular view as guided by refs. 14 and 15.

2.1 π-Conjugated Molecules

An isolated carbon atom has the ground state electron configuration: $1s^2 2s^2 2p_x^1 2p_x^1$. When two carbon atoms forms a bond the 2s and $2p_{x/y}$ orbitals hybridizes in such a way that the chemical bonds are equivalent and energetically degenerate. This is what causes symmetrical molecular structures such as fullerenes. When each carbon atom has three binding partners, the individual carbon atom forms three orbitals that are linear combinations of a $2s$-orbital the $2p_x$-orbital and the $2p_y$-orbital. This is referred to as sp^2 hybridization. Overlapping sp^2 orbitals of neighbouring carbon atoms results in relatively strong molecular binding orbitals localised in the molecular plane which are usually denoted by σ. The corresponding molecular anti-bonding orbital is denoted by σ^*. The remaining valence electron not participating in hybridized bonding, then changes from a $2s$-state to a $2p_z$-state which is oriented perpendicularly to the molecular plane. Analogous to the formation of σ orbitals, the overlap of two bonding $2p_z$-orbitals forms molecular bonding orbitals and the overlap of two anti-bonding $2p_z$-orbitals forms molecular anti-bonding orbitals called π and π^* respectively. This result of an organic molecule where the carbon atoms have three binding partner each, such as Polyacetylene or the carbon backbones of P3HT and PCBM is therefore double bonds between carbon atoms. However, a molecular configuration where the bond lengths between all carbon atoms are identical turns out to be unstable. This can be understood as follows: If some amount of extra energy is brought to the molecule which causes an elastic deformation and thereby alternating longer and short bonds, a periodic potential for the π-electrons is created. This periodic potential opens up a gap, which with Brillouin theory can be seen to imply that there are two π-orbitals corresponding to different energies which have the same wavenumber. The one orbital has maxima between the longer bonds, and the second orbital has maxima between shorter bonds. The latter is associated with a lower energy than the former since an electron in that state in average is at a shorter distance from the nuclei and therefore more stable. This is known as Peierls instability[16] and causes the carbon atoms to form alternating single and double bonds between them. Single bonds are constituted of overlapping σ orbitals while overlapping σ orbitals and π-orbitals between two atoms constitutes double bonds. A molecule with alternating double and single bonds are said to have a conjugated electron system, in this case π-conjugated. The π and $\pi*$ orbitals are less bonding and anti-bonding than the σ-bonds because they overlap less, thus forming the frontier orbitals: In the ground state of an organic molecule with three bonds per atom, the highest occupied molecular orbital (HOMO) is the π orbitals followed by the σ-orbitals while the lowest unoccupied molecular orbital, (LUMO) is the anti-binding π^* orbital followed by the anti-binding σ^* orbitals. This is shown in Fig. 2.1 below. The energy gab, E_g, between the HOMO and the LUMO is determined by the degree of delocalisation of the π orbitals. For P3HT, $E_g = 1.9$ eV. In fact, the π electrons are generally delocalised to a large degree in π-conjugated molecule, which is the root to the high charge mobilities and resulting semiconducting behaviour.

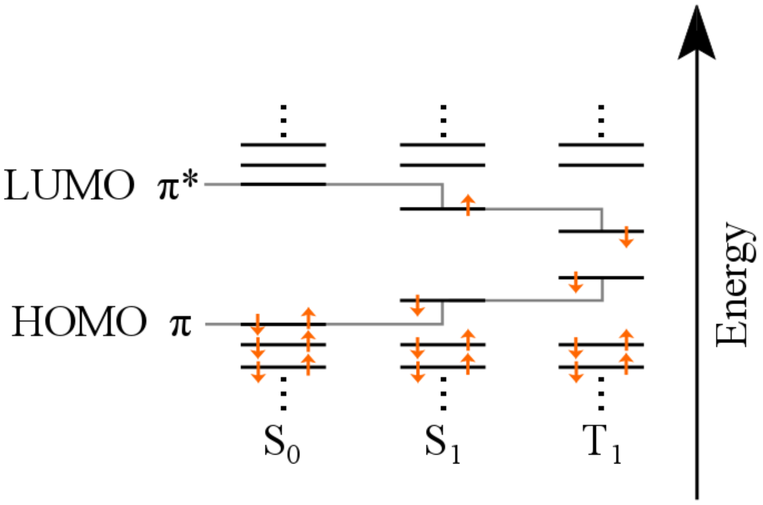

Figure 2.1: Electronic configuration of the ground state,S_0, the first singlet-spin excited state, S_1, and the first triplet-spin excited state, T_1, where coulomb and exchange energies are included in the positions of the frontier orbitals. The arrows indicate electrons and the direction indicates the value of the electron spin. Adapted from [17]

.

In an organic molecule, neutral excited states can be formed in optical transitions. If a photon that matches the energy difference between the HOMO and the LUMO is absorbed by one of the electrons in the HOMO and thereby promoting it to the LUMO, a neutral excited state is formed, which is refereed to as an exciton. In general, any configuration with an electron in an anti-bonding orbital and a missing electron in a bonding orbital, i.e. a hole, is a neutral excited state. It is important to distinguish between those excitons where the total spin is zero, and those where the total spin is one. The former is called a singlet exciton, because there is only one value for the spin's projection on the z-axis, $m_s = 0$. The latter is created through interaction between singlet excitons and is referred to as a triplet exciton because there are three possible values for $m_s = \pm 1, 0$. Singlet excitons decay to the ground state radiatively, while this is forbidden for triplet excitons due to spin selection rules. Molecular orbital diagrams corresponding to the configurations in the ground and first neutral excited states are presented in Fig. 2.1 and the nature of excitons is elaborated in the following section.

2.2 Neutral Excited States

Neutral electronic excited states in an organic semiconductor are generally referred to as excitons. The unoccupied molecular orbital the electron is excited to, can be in the same molecule or a neighbouring one.

In inorganic semiconductors the so called Mott-Wannier excitons are formed. Here, a high dielectric constant compared to organic semiconductors, $\varepsilon_{inorg} \approx 11$ and $\varepsilon_{org} \approx 3$[17], means that screening of Coulomb forces are more efficient than it is for organic semiconductors. Small attractive forces between hole and electron results in excitons with small binding energy, E_B, and thus large spatial extend. The diameter of the special extend of Mott-Wannier excitons is typically one order of magnitude larger than the lattice constant. Furthermore, E_B is on the order the thermal energy of the material at room temperature. This means that Mott-Wannier are dissociated much faster than their average lifetime. In organic semiconductors, Mott-Wannier excitons have yet to be observed due to low dielectric constants. Instead, the excitons have such high binding energy, usually in the order of 100 meV, that thermal excitations at room temperature, $k_B \cdot 300\text{K} = 25$ meV, is not sufficient for separating the electron-hole pair. The high E_B also means that the diameter of the exciton is comparable with the largest dimension of the molecules. Excitons with extensions comparable with the molecules of a molecular crystal is referred to as Frenkel excitons. A little lower in the E_B-spectrum than Frenkel excitons are the so called charge transfer (CT) excitons. The extend of these excitons are comparable with the lattice site separation, and the electron and the hole are therefore effectively located in two different molecules.

Exciton Migration

When the electric field inside an organic semiconductor crystal is homogeneous there is no external force on the excitons in it. In that case the migration of excitons within the crystal is entirely due to diffusion. This diffusion is the result of a large sum of exciton energy transfers from one molecule to another, effectively being a stochastic process of hopping between lattice sites referred to as random walking. Singlet Frenkel excitons commonly transfer through Förster resonant energy transfer (FRET) [18]. FRET is based on resonance theory of energy transfer and is due to dipole-dipole interactions between identical molecules. The process goes as follows: A singlet exciton on a molecule recombines radiatively and the emitted photon is reabsorbed by another identical molecule creating an exciton in it. The rate of FRET, k_{FRET} is inversely proportional to the lifetime, τ, of the exciton and the distance between the two molecules, R, to the sixth power:

$$k_{FRET} \propto \frac{1}{\tau} \cdot \frac{1}{R^6}$$

A good concept for describing the resulting diffusion is the diffusion length, L_D, which is the distance between the starting point and the end point of the exciton diffusion path. Assuming isotropic hopping motion, L_D can through the diffusion coefficient, D, a dimensional parameter, Z, and the exciton lifetime, τ, be expressed as

$$L_D = \sqrt{Z \cdot D \cdot \tau} \tag{2.1}$$

Z equals 2,4 or 6 for one-, two-, and three-dimensional crystal respectively. For Anisotropic crystals, which most organic molecular crystals are, different diffusion coefficients are ascribed to the different directionalities in the crystal. The diffusion coefficient is proportional to the mobility of the exciton, μ_{ex}, as given by the Einstein relation:

$$D = \mu_{\mathrm{ex}} \cdot k_B \cdot T \tag{2.2}$$

Here T is temperature and k_B is Boltzmann's constant. Exciton diffusion is very important in organic solar cells, the interface between the donor phase and the acceptor phase needs to be reached before the exciton decays in order to separate it into charges.

2.3 Charged Excited States

For charge transport to occur in organic semiconductors, there must be free electric charges which are mobile. As in inorganic semiconductors, there are two species with potential for contributing to charge transport: electrons accommodated in an anti-bonding orbital and vacancies in the bonding orbitals which are referred to as *holes*. Such species can be achieved in three ways: (1) By injection or extraction of an electron at the interface between a metal electrode and the molecule. (2) Though reduction or oxidation of the molecule by a donor/acceptor molecule. (3) Through dissociation of a neutral excited state in a molecule by electron transfer to an adjacent molecule. The latter process leads to geminately bound electron-hole pairs as precursors for free positive and negative charges in organic solar cells.

From electrochemical experiments it is well known that the removal of a second electron from a molecule requires more energy than the the energy required for removing the first electron [17]. This is because the equilibrium geometry in the ionized state is different form that in the ground state. A simplified picture of the potential energy wells of the ground state and the first ionized state for an organic molecule along with energies involved in the ionization process is shown in Figure 2.2.

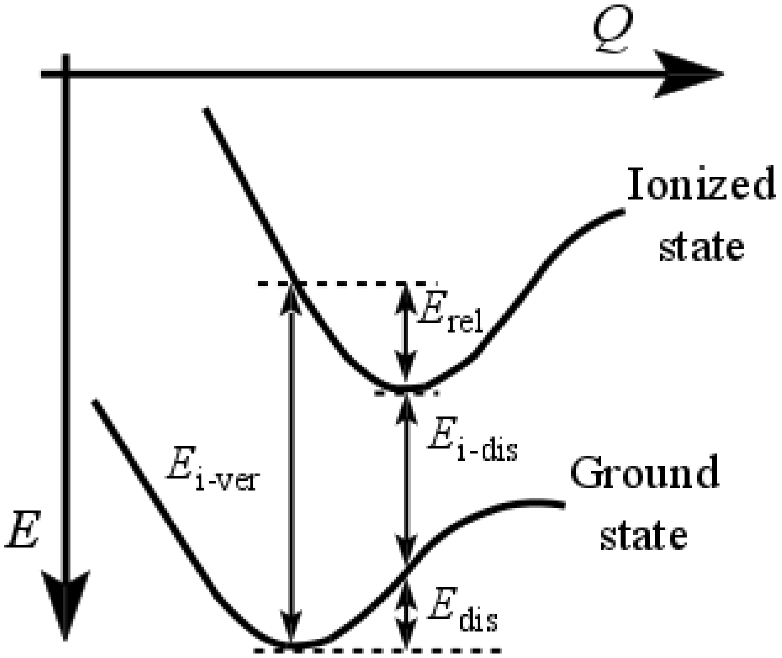

Figure 2.2: Energies involved in ionization of a molecule. Along the axes are E, the potential energy of the molecule, and Q, a parameter representing variation in the molecular geometry of the molecule. $E_{\text{i-ver}}$ is the vertical ionization energy. E_{rel} is the relaxation energy saved by distorting in the ionized state. E_{dis} is the distortion energy is the energy the molecule pays to distort in the ground state. $E_{\text{i-dis}}$ is the ionization energy of the distorted molecule.

Consider the vertical ionization process which costs an energy $E_{\text{i-ver}}$. If the ionized state relaxes, the molecule gains back a relaxation energy E_{rel}. This process can also be thought of as the ground state molecule distorting such that it has the equilibrium geometry of the ionized state at the cost of an elastic distortion energy E_{dis} before ionization occurs at the cost of $E_{\text{i-dis}}$. Therefore, distortion of the molecule in the ionized state occurs if

$$E_{\text{dis}} < E_{\text{i-ver}} - E_{\text{i-dis}} = E_{\text{dis}} + E_{\text{rel}} \Leftrightarrow E_{\text{dis}} < E_{\text{rel}} \tag{2.3}$$

In other words, the promotion of an electron from a π-orbital to a π^*-orbital changes the spatial distribution of electrons in the σ-orbitals if the inequality (2.3) is true. This results in new bond lengths of the molecule. The energy associated with this change in molecular geometry is called the geometric organization energy, and the charge in conjunction with the geometric distortion of the molecule is known as a polaron. This effect is important in organic semiconductors while absent in inorganic ones where the strong dielectric screening negates them. The polaronic states are located in the band-gap of an organic semiconductor. This can be seen from Figure 2.2, where the HOMO is shifted to higher energy and the LUMO is shifted to a lower energy. This is really not surprising, since the electronic states are localized to the distortion, and hence cannot move around freely. Consider now the removal of a second electron from the organic semiconductor. It can either be energetically favourable to take the second electron from the polaron or to take it from another location in the organic semiconductor. In the latter case, two polarons are formed. In the former case, a so called bipolaron is formed, which is defined as a pair of like charges associated with a single lattice distortion. Since the degree of lattice distortion around two charges is larger than for one charge, E_{dis} for a bipolaron is larger than E_{dis} for a polaron. This causes the electronic states in the band-gap to be further away from the band edges for a for a bipolaron than for a polaron.

Charge Transport

Charge transport in organic semiconducting crystals is a complex matter due to a relatively high degree of disorder in them. As mentioned in Sec. 2.1, the mobility of charge carriers is tied up to the degree of delocalisation of the π-electrons. Molecular stacking of planar molecules such as DBP and P3HT leads to increased overlap of π-orbitals and therefore more delocalised π-electrons. However, in reality the degree of disorder is always sufficiently high such that charges cannot be viewed at being localised over more than a few molecules. At the very least, the deformation of the molecular unit of an organic semiconductor in its ionized sates tends to localise charges in the solid. Therefore, charge transfer from molecule to molecule, so called hopping, is is an essential part of understanding charge transport in organic semiconductors.

Chapter 3

Organic Solar Cells

While still far from practical stability under operation[7] and no immediate technique for large-scale fabrication available, solution processed solar cells with active layers comprised of phase separated donor/acceptor blends, bulk heterojunctions (BHJs), is the leading technology in solar cell efficiency and overall the best type of OSC. This chapter introduces solar cells based on the BHJ and in particular P3HT:PCBM ones.

3.1 Basic Function and Development of Organic Photovoltaic Cells

A layer of organic electronic material between a high work function conductor, typiccaly indium tin oxide (ITO), and a low work function metal such as aluminium, will serve as a photovoltaic cell (PVC)[19, 20]. The so called single layer PVC relies on the electric field between the electrodes to split excitons in the organic semiconductor. The small probability of this to happen due to the high binding energy of the Frenkel excitons is reflected in the 10^{-3} % to 10^{-2} %[5] power conversion efficiency (PCE) of the first generation of OSCs made in this way. The next generation of devices feature a planar heterojunction. Here, a film of a material acting as an electron donor and a film of material acting as an electron acceptor are sandwiched between the contacts. The acceptor has the higher electron affinity and ionization energy than the donor. This relationship which makes it energetically favourable for hole to reside at a donor molecule and an electron to reside at an acceptor molecule. Additionally, it creates an electric field at the interface between the acceptor and donor films. The hole conducting contact is typically ITO while the electron conducting contact is Aluminium.

The planar heterojunction OSC suffer from a large distance between the site of the average exciton to the donor/acceptor interface. Due to the local electric field, charge separation at the donor/acceptor interface is very efficient in converting photogenerated Frenkel excitons into polarons[21]. In fact, the charge separattion at the interface has experiemntially been determined to happen faster than 100 fs [22]. However, it is also the only effective mechanism for separating the charges. Thus, a planar heterojunction device needs to have a donor layer of thickness similar to the exciton diffusion length in typical organic semiconductors which is $3 - 10$ nm. This is an inherent problem, since the ability to absorb light decreases with the thickness of the donor layer.

Bulk Heterojunction

The bulk heterojunction (BHJ) devices addresses the problem of limited exciton diffusion outlined above. Here, the donor and acceptor molecules are dissolved in the same solution before they are cast onto the sample. In the effective BHJ, the donor and acceptor molecules are then brought to phase separate in a percolated network with donor phases of ~ 10 nm. The thickness of the active layer in BHJ solar cells can thus be larger than the exciton diffusion length. Typically, they are made with thickness ~ 100 nm. The type of solar cells under investigation in this project is of the BHJ-type. In particular, the polymer donor P3HT is considered in combination with PCBM as acceptor.

3.2 P3HT Solar Cells

This section describes the important aspects of solar cells based on the polymer solar cells based on the electron donor poly(3-hexylthiophene)(P3HT) and the electron acceptor PCBM.

For P3HT, the 3-hexyl substituent in a thiophene ring has two ways for which it can be incorporated into a polymer chain , namely head-to-head (HH) and head-to-tail (HT). A polymer chain having either of the two configurations is called regioregular (RR). When a chain has sequences of each type of 3-hexyl incorporation, it is said to have a certain degree of regioregularity. When the length of the sequences become sufficiently short, the polymer is said to be regiorandom (RRa). Of particular importance, with regards to OSCs, is the regularly substituted poly(3-hexylthiophene) (RR-P3HT), in which the hexyl side chain is attached to the third position of a thiophene ring in an HT regioregularity [23]. This is because self-organization of RR-P3HT chains result in two-dimensional (2D) lamella nanostructures which tend to stack to form a three-dimensional crystalline structure. In the 2D nanostructures, the interchain distance is as short as ~ 3.8Å[24] and therefore the interchain interaction is large compared with RRa-P3HT. The strong interchain interactions in RR-P3HT cause the singlet excitons to be of the localised over multiple polymer chains, i.e. charge transfer excitons, whereas only Frenkel excitons are formed in RRa-P3HT films. Likewise, long-lived polarons are also delocalized over multiple adjecent chains in RR-P3HT films, giving rise to both interchain and intrachain polarons, while only interchain polarons are formed in RRa-P3HT.[24] In turn, this causes a larger exciton and polaron mobility in the RR-P3HT.

3.2.1 P3HT:PCBM Bulk Heterojunctions

The usual acceptor used in conjunction with polymer donors is fullerene, either C_{60} or C_{70}. Their derivative, [6,6]-phenyl-C(61/71)-butyric acid methyl ester (PCBM), is however often used since its side chain makes it easier to dissolve in chlorobenzene. The electron affinities and ionization energies of PCBM and P3HT along with schematic representations of their molecular structures are shown in Fig. 3.1 below.

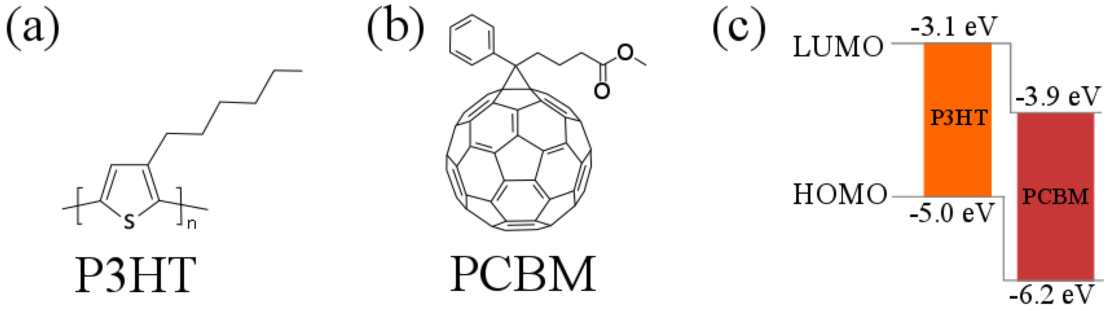

Figure 3.1: Molecular structure of P3HT (a) and P3HT (b)along with their band-edge energies.

In the pristine P3HT:PCBM blend films, the molecules are not phase separated. Instead, PCBM nanocrystals are uniformly spread throughout a disordered P3HT matrix.

Annealing changes this situation. The nanostructure of annealed RR-P3HT:PCBM films have been studied via transmission electron microscopy and electron diffraction [25, 26, 27]. The studies show three phases in the films:

- Fibrillar network of P3HT crystals
- Aggregates of PCBM nanocrystals
- Relatively disordered P3HT matrices with PCBM nanocrystals in them

The annealed solar cell is more efficient than the pristine. Upon annealing, the effeciency of P3HT:PCBM solar cells external quantum efficiency at peak absorption has been measured to increase from 30 % for pristine to 55% for annealed [28]. This is attributed to the phase separation and the resulting networks of crystalline P3HT and PCBM aggregates.

Chapter 4

Supercontinuum Generation

A essential part of the investigation of the P3HT:PCBM system, is the optical probe pulse used to measure the absorbance of the samples in the transient absorption experiment described in Ch. 5. This pulse is the result of extensive spectral broadening of a narrow-band 786 nm femtosecond seed pulse into a broad-band pulse covering the visible and a part of the near infrared by propagation through a sapphire window. This is a known process referred to as supercontinuum generation (SCG) [29]. The key to this spectral broadening is self-phase-modulation of the high intensity seed pulse due to a nonlinear index of refraction, n_2, of the optical medium ($n_2 = 3.1 \cdot 10^{-16}$ cm^2/W for sapphire [30]).

In order to understand the phenomenon and control it in the laboratory, an introduction to a simple description of the phenomenon is useful. Thus, this chapter introduces the basic phenomenons at play in supercontinuum generation.

4.1 The Nonlinear Electric Susceptibility

The third order nonlinear term in the polarizabilty of optical media is the origin of spectral broadening of the probe pulses. This section introduces the nonlinear polarizabilit and its interaction with an applied optical field.

When light propagates in a medium, the medium responds to the electric field of the light by forming electric dipoles. The electric dipole moment per unit volume, also known as the polarization, P, in a material can be expressed as a power series expansion in the electric field amplitude, E:

$$P = \epsilon_0 \chi^{(1)} E + \epsilon_0 \chi^{(2)} E^2 + \epsilon_0 \chi^{(3)} E^3 + \cdots \tag{4.1}$$

Here, the coefficient for the n'th order term in the expansion has been written as the product of two physical quantities, namely the electric permitivity for free space, ε_0, and the n'th order electric susceptibility $\chi^{(n)}$. When E is sufficiently small, the nonlinear terms are negligible compared to the the linear term. When E is large, the nonlinear terms become important. This is the area of nonlinear optics.

The χ's in Eq. 4.1 are responsible for different optical phenomena.

- $\chi^{(1)}$ describes linear optics, e.g. how lenses work.
- $\chi^{(2)}$ describes second-order effects, e.g. second-harmonic generation
- $\chi^{(3)}$ describes third-order effects, such as third-harmonic generation and the intensity dependence of the index of refraction

Since the polarization in the linear domain is just a scalar multiple of the field, the two vectors has the same direction. In general, for media that respond instantaneously to an applied electric field, the length of the polarization vector is described through a power series in the strength of the field

4.1.1 Intensity Dependence of the Refractive Index

For many optical materials, the refractive index depends upon the intensity of the light propagating through it. For these materials, the total refractive index can be written as

$$n = n_0 + n_2 I \tag{4.2}$$

where n_0 is the usual refractive index for weak electromagnetic fields, and n_2 is an optical constant referred to as the nonlinear index of refraction. n_2 can be interpreted as the rate at which the refractive index changes as the time-averaged intensity, I, increases. The change in refractive index with light intensity is sometimes called the optical Kerr effect, after the traditional Kerr electrooptic effect, where an applied static electric field changes the refractive index of the material.

4.2 Self-Phase Modulation

The Generation of supercontinuum laser pulses resulting from modification of a laser pulse by a optical medium, was first reported by Alfano and Shapiro in 1970. The measured frequency broadening in crystals and glasses, when they shot 4 ps laserpulses into sapphire and Calcite. Self-phase modulation was here responsible for the frequency broadening. The physical mechanism for the modulation of the frequency is change in the refractive index due to distortion of the electron cloud. In solids, mechanisms giving rise to the coefficient of the intensity dependent refractive index, n_2, are for picosecond pulse excitation either direct distortion of electronic clouds around nuclei or one of several coupled electronic mechanisms: librational distortion where electronic structure is distorted as the molecule rocks, electron-lattice distortion where the electron cloud distorts as the lattice vibrates, and molecular redistribution where electronic shells are altered as the nuclei redistribute spatially. [29]

A description of self-phase modulation as guided by [29], follows here. In order to describe the basic mechanism of self-phase modulation in a simple manner, the nonlinear wave equation can be examined under a list of approximations: Linearly polarized electric field, slowly varying envelope, homogeneous radial fields, isotropic and nonmagnetic medium, gegligible Raman effect, frequency-independent $\chi^{(3)}$, and neglect of group velocity dispersion, absorption, self-steepening and self-frequency shift.

Being an electromagnetic field, the laser pulse in the sapphire obeys Maxwell's equations:

$$\nabla \times \vec{E}(\vec{r},t) = -\frac{\partial \vec{B}(\vec{r},t)}{\partial t} \qquad \text{(Law of Ampere)} \tag{4.3}$$

$$\nabla \times \vec{H}(\vec{r},t) = \frac{\partial \vec{D}(\vec{r},t)}{\partial t} + \vec{J}(\vec{r},t) \qquad \text{(Law of Faraday)} \tag{4.4}$$

$$\nabla \cdot \vec{D}(\vec{r},t) = \rho(\vec{r},t) \qquad \text{(Gauss' law of electricity)} \tag{4.5}$$

$$\nabla \cdot \vec{B}(\vec{r},t) = 0 \qquad \text{(Gauss' law of magnetism)} \tag{4.6}$$

$\rho(t)$ is the density of free electric charge and $\vec{J}(t)$ is the current density vector. Using the constitutive relations

$$\vec{D}(\vec{r},t) = \epsilon_0 \vec{E}(\vec{r},t) + \vec{P}(\vec{r},t) = \varepsilon \vec{E}(\vec{r},t) \quad \text{and} \quad \vec{B}(\vec{r},t) = \mu_0 \left(\vec{H}(\vec{r},t) + \vec{M}(\vec{r},t) \right) = \mu \vec{H}(\vec{r},t)$$

the equations 4.3 and 4.4 can be reduced to a single first order partial differential equation governing the complex pulse envelope, $A(z,t)$. By writing the total refractive index as $n = n_0 + n_2|\vec{E}|^2$ and neglecting n_2^2-terms, the partial differential equation for A, in Gaussian units, is

$$\frac{\partial A}{\partial z} + \frac{1}{v_g}\frac{\partial A}{\partial t} = i\frac{\omega_0 n_2}{2c}|A|^2 A \qquad (cgs) \tag{4.7}$$

where $v_g = 1/\left(\partial k/\partial \omega\right)$ is the group velocity. Denoting its phase by ϕ, the complex pulse envelope in polar form is $A = |A|e^{i\phi}$, and equation 4.7 reduces to

$$\frac{\partial |A|}{\partial z} + \frac{1}{v_g}\frac{\partial |A|}{\partial t} = 0 \tag{4.8}$$

and

$$\frac{\partial \phi}{\partial z} + \frac{1}{v_g}\frac{\partial \phi}{\partial t} = \frac{\omega_0 n_2}{2c}|A|^2 \tag{4.9}$$

Equations 4.8 and 4.13 has the solutions

$$|A(\tau)| = |A|_0 F(\tau) \tag{4.10}$$

and

$$\phi(z,\tau) = \frac{\omega_0 n_2}{2c}\int_0^z |A|^2 dz' = \frac{\omega_0 n_2}{2c}|A|_0^2 F(\tau)^2 z \tag{4.11}$$

where $|A|_0$ is the amplitude, $F(\tau)$ is the pulse envelope, and τ the local time $\tau = t - z/v_g$. In the case of materials with response times slower than than pure electronic but still faster than molecular orientation, the envelope is just the optical pulse shape. For a pure electronic response, the envelope should include the optical cycles in the pulse shape. The electric field envelope given by Eq. 4.7, is thus:

$$A(z,\tau) = |A(\tau)| \exp\left(i\frac{\omega_0 n_2}{2c} a_0^2 F(\tau)^2 z\right) \tag{4.12}$$

Equation 4.12 contains the main physics of self-phase modulation. Since n_2 depends on intensity, it changes with time as the pulse propagates. This leads to a time-dependence of the phase of the pulse due to its own distortion of the nonlinear medium, resulting in self-phase modulation. Since the slowly varying amplitude approximation is adopted, the duration of the pulse is much larger than the optical period $2\pi/\omega_0$. In that case, the electric field at each position τ within the pulse has a *local* and *instantaneous frequency*

$$\omega(\tau) = \omega_0 + \delta\omega(\tau) \tag{4.13}$$

where

$$\delta\omega(\tau) = -\frac{\partial\phi}{\partial\tau} = -\frac{\omega_0}{2c} n_2 a_0^2 z \frac{\partial F(\partial\tau)^2}{\partial\tau} \tag{4.14}$$

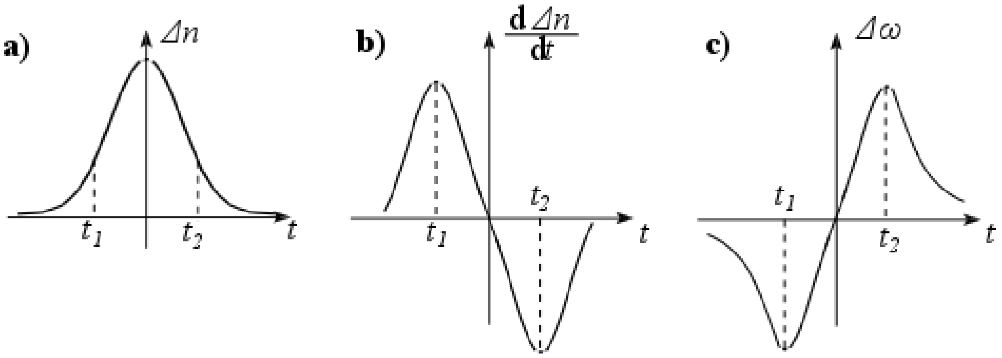

Figure 4.1: SPM for a symmetric laser pulse: (a) time-dependent nonlinear index change, (b) time rate of change of index change, (c) time distribution of SPM-shifted frequencies. Adapted from [29]

The Fourier transform of $A(z,\tau)$ gives the spectrum of the self-modulated pulse:

$$A(\Omega) = \frac{1}{2\pi}\int_{-\infty}^{\infty} A(z,\tau) e^{i\Omega\tau} d\tau \tag{4.15}$$

Here, $\Omega = \omega - \omega_0$. The intensity spectrum,

$$\frac{c}{4\pi}|A(\Omega,z)|^2 \ , \tag{4.16}$$

can then be calculated. For a Gaussian envelope function

$$F(\tau) = e^{2\sqrt{2\ln(2)}\tau^2/\Sigma^2} \tag{4.17}$$

with full width at half maximum (FWHM), $\Sigma = 100$ fs and

$$\beta \equiv \frac{n_2|A|_0\omega_0}{2c}z = 30 \tag{4.18}$$

the spectrum of the output shows a broadening of several hundred cm^{-1} with a quasiperiodic oscillation [29]. Since the SPM pulse, $\Delta\phi$, is symmetric, the output spectrum is symmetric around the frequency of the incoming laser frequency. The leading half of the SPM pulse is responsible for the Stokes broadening and the lagging half is responsible for the anti-Stokes broadening. Since the SPM pulse takes on a bell shape, one can always find another point with the same slope as some given point. This is with the exception of the infliction points. As $\partial\phi/\partial\tau = -\omega$, such two points with identical slope describe radiated waves of the same frequency but different phases. Those two waves interfere constructively if the phase difference $\Delta\phi_{12}$ is and integer multiple of 2π and destructively if $\Delta\phi_{12}$ is and odd integer multiple of π. This interference gives rise to the peaks and valleys in the calculated spectrum. The two outermost peaks with $|\omega_{\max|\sim|\partial\phi/\partial t}|_{\max}$ correspond to the infliction points where the SPM pulse has its largest slope. The number of peaks on each side of the spectrum is found as the number of pairs of constructive and destructive interferences, $N \sim \phi_{\max}/2\pi$. The broadened spectrum has Stokes-anti-Stokes symmetry because $\Delta\phi(t)$ is directly proportional to $|E(t)|^2$ and is a symmetric pulse. For the general case where not instantaneous, one has

$$\Delta\phi(z,t) = \frac{\omega}{c}\int_0^z \Delta n(z,t)dz \tag{4.19}$$

$$\Delta n(z,t) = \int_{-\infty}^{z} n_2(z,t-t')|E(z,t')|^2 dt' \tag{4.20}$$

where $n_2 = (2\pi/n_0)\chi^{(3)}(z,t)$.

4.3 Filamentation

Self-action effects are effects in which a beam modifies its own propagation due to the nonlinear response of a material medium. self-phase modulation is one example of such, self-trapping is another example. Self-trapping and the resulting filamentation, turns out to be crucial in the process of supercontinuum generation, unless taking advantage of an optical fiber. This section describes a basic theory of filamentation via self-focusing as outlined by ref. 31.

Self-trapping of light refers to the situation where a beam of light propagates with a constant diameter as a consequence of a balance between a process called self-focusing and diffraction effects. The process of self-focusing is when an intense light-beam modifies the optical properties of a material medium such that the beam comes to focus within the material as the result. In particular, it happens when the second order nonlinear refractive index, n_2, is positive. A positive n_2 induces a refractive index variation in the material, where the refractive index is larger in the center of the beam than in its perimeter. This causes the material to act as a postive lense, causing the beam to come to a focus within the material. As it focuses, the intensity of the beam increases further enhancing the self-focusing effect, which further increases the intensity etc.. The situation is shown in Figure 4.2-**(a)**

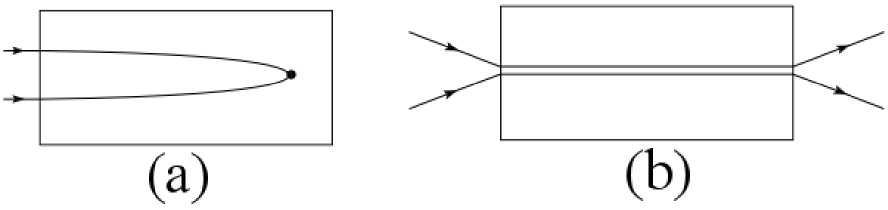

Figure 4.2: Intense light beams entering material media with $n_2 > 0$. in **(a)** a collimated beam is self-focused, and in **(b)** a converging beam is being self-trapped by the material medium.

At a critical power, P_c, the tendency of the beam to diffract exactly balances the the tendency to self-focus, and self-trapping of the beam is achieved. This is shown in Fig. 4.2-**(a)**.' Figure 4.3 shows a collimated beam of light with on-axis intensity I_0 incident on a nonlinear optical material with $n_2 > 0$.

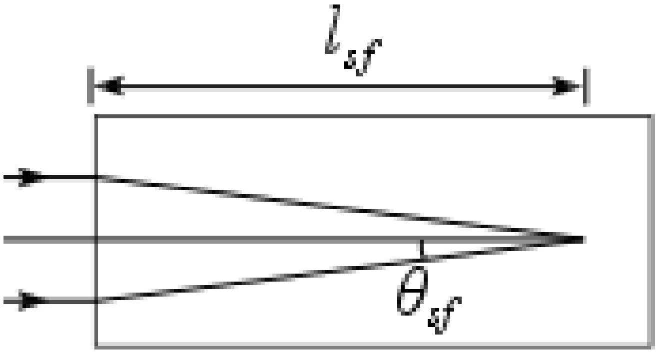

Figure 4.3

The angle at which the beam converges into a self-focus, θ_{sf}, can be described by applying Fermat's principle, which states that the optical path length $\int n(\vec{r})dl$ of any two rays traveling from the wavefront at the input interface of the material medium to the self-focus must be equal. As a first estimate the approximation that $n = n_0$ along the marginal ray and $n = n_0 + n_2 I_0$ along the central ray. Then, Fermat's principle states that

$$(n_0 + n_2 I)\, z_{sf} = \frac{n_0 z_{sf}}{\cos\theta_{sf}} \tag{4.21}$$

Approximating $\cos x \approx 1 - \frac{1}{2}x^2$, which is reasonable for small x, Eq. 4.21 gives that

$$\theta_{sf} = \sqrt{2n_2 I/n_0} \tag{4.22}$$

The condition for self-trapping is then that the diffraction angle of the beam is equal to the self-focusing angle. That is $\theta_{\text{dif}} = \theta_{\text{sf}}$, where

$$\theta_{\text{dif}} = 0.61\lambda_0/n_0 d \tag{4.23}$$

is the diffraction angle of a beam with diameter d, and vacuum wavelength λ_0. By equating the right hand sides of Eqs. 4.21 and 4.23, it is found that self-trapping occurs when only if the intensity of the light within the filament is exactly

$$I = \frac{0.61^2 \lambda_0^2}{2n_2 n_0 d^2} \tag{4.24}$$

Now, the power contained in such a filament is exactly the power that must be contained in the beam in order to achieve self-trapping, P_{cr}:

$$P_{cr} = \frac{\pi}{4} d^2 I = \frac{\pi 0.61^2 \lambda_0^2}{8 n_0 n_2} \approx \frac{0.15\lambda_0^2}{n_0 n_2} \tag{4.25}$$

When the power in the incident beam greatly exceeds P_{cr}, the beam will tend to break up into several filaments, each of which contains power P_{cr}.[31]

Chapter 5

Transient Absorption Spectroscopy on P3HT:PCBM

Transient absorption spectroscopy is an optical pump-probe technique where the change in absorbance due to excited states is measured by pumping the sample optically prior to measuring the absorbance of it. Mode-locked lasers with pulse lengths on the femtosecond time scale, allows this technique to detect and resolve the decay of excited states which have lifetimes of picoseconds. In fact, optical pump-probe spectroscopy is fastest detection technique available. The timely resolution is limited by the pulse length of the laser, which can be as short as attoseconds.

The transient absorption spectrum of a BHJ solar cell in the visible to near-infrared can be used to study the efficiency of the cell. For example,the fraction of excitons which reaches the donor/acceptor interface and successfully charge separates can be found by comparing the initial exciton density to the density of polarons after the excitons have decayed. This can be done since the transient change in absorption caused by excited states in the samples is related to the density of these states. This chapter describes the experimental set-up produced with the purpose of studying the efficiency of basic photovoltaic processes in P3HT:PCBM bulk heterojunction solar cells. This is followed by a brief description of the transient absorption spectrum expected in P3HT and P3HT:PCBM within the first ns of the excitation.

5.1 Experimental Set-Up

The absorbance change of P3HT and P3HT:PCBM has in this project been measured as a function of delay-time between the pump- and the probe-pulse at selected wavelengths. This was done via transient absorption spectroscopy in transmission mode using an experimental set-up arranged by the author on an optical table. An overview of the set-up is shown in Fig. 5.1.

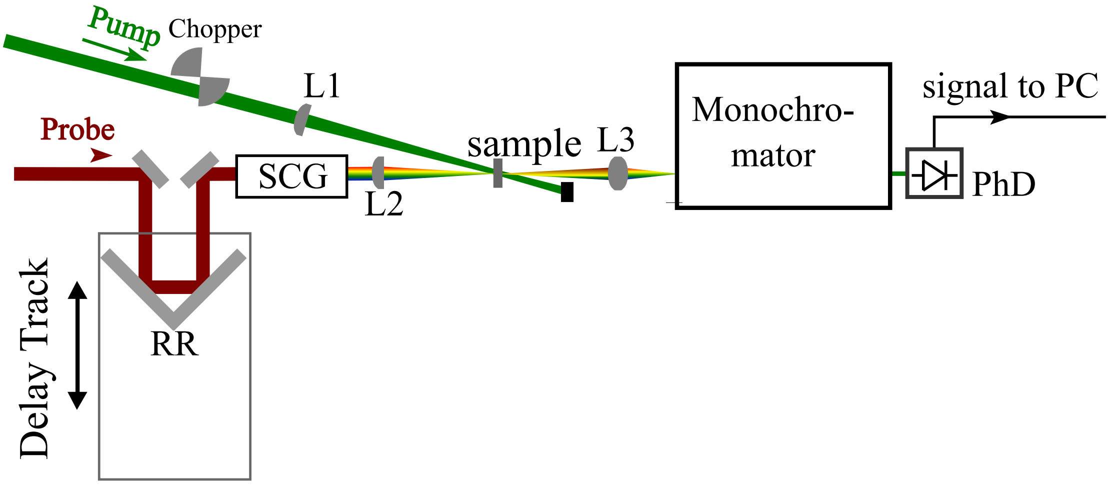

Figure 5.1: Experimental set-up used fr the measurements of Ch. 6. "L1" ($f_1 = 1000$ mm), "L2" ($f_2 = 200$ mm) and "L3" ($f_3 = 50$ mm) are plano-convex lenses. "SCG" refers to supercontinuum generation. "RR" is a retroreflector and "PhD" is a photodiode detector.

The pump and probe pulses originate from ~ 100 fs pulses generated in a Quantronix Integra-C amplifier [32] which is seeded by 786 nm pulses from a Tsunami Ti:sapphire mode-locked laser [33]. The Integra-C increases the peak intensity of the incoming pulses via chirped pulse amplification in a Ti:Sapphire crystal. The nonlinearity in the Ti:sapphire crystal causes self-focusing of the pulses as described in Sec. 4.3. This can result in permanent damage to the crystal if the intensity of the beam is too high (10GW/cm^2). Therefore, the seed pulses are stretched by a grating before amplification in the Ti:sapphire in order to decrease the peak intensity. After amplification, the pulses are compressed to their original duration. This allows for amplification of Tsunami seed pulse by up to a factor of $80 \cdot 10^3$. For the measurements in this project, the resulting output of the Integra-C is a 1 kHz train of 2.5 mJ pulses in a collimated beam with a full width at $1/e^2$ maximum of ~ 7 mm (Gaussian fit)[32].

The Integra-C pulse train is split by a semitransparent mirror, which directs the reflected part (80 %) to a Tunable Optical Parametric Amplifier (TOPAS) in which the pump pulses are generated. The other 20 % is led through a 3 mm thick sapphire window where the frequency-spectrum of the pulses are broadened by the process of self-phase modulation, i.e. supercontinuum generation, as described in Ch. 4. The pulses delivered by the Integra-C, is focused with a spherical mirror with focal length $f_s = 8$ cm into the sapphire crystal, to start the continuum generation (SCG). Since the position of the focus with respect to the sapphire is important for the effectiveness of the SCG, the sapphire is placed on a translation stage. Before the focusing mirror, an iris is placed to regulate the effective diameter of the mirror and thus the numerical aperture of the SCG-arrangement.

The pulses are reduced in power by, first, a neutral density (ND) filter and secondly a polarizer. The ND-filter serves to avoid the risk of damaging the sapphire crystal. With the polarizer, one is allowed to tune the power incident on the sapphire such that SCG is optimal. A schematic representation of the supercontinuum generation arrangement is shown below in Figure 5.2 **(a)**

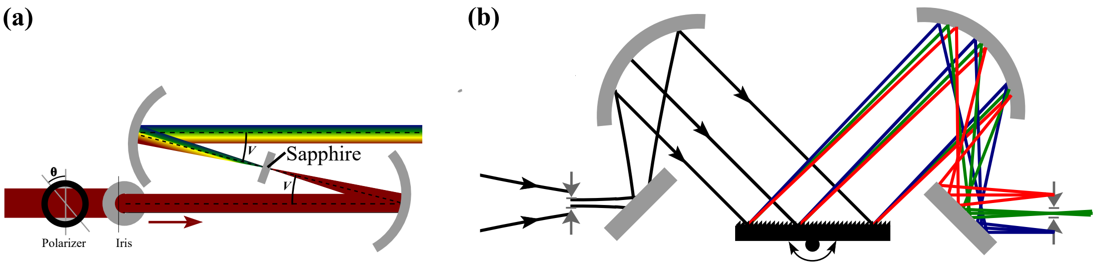

Figure 5.2: The sub-arrangement for supercontinuum generation (a) and the beam path inside the monochromator (b).

The pulse train resulting from SCG in the sapphire window is used as probe with regards to the measurements of absorbance change of the samples. Each pulse contains a continuous spectrum with wavelengths reaching from ,∼ 450 nm to ∼ 1100 nm. This is documented by the measured spectrum of the pulses which is presented in Sec. 5.1.1. Once the probe pulses have been transmitted through the sample, they are picked up by a monochromator in order to select the wavelength at which the transient absorption kinetics is to be measured. In the monochromator, a reflective blazed diffraction grating optimized for 1250 nm light is used to separated the frequency-components of the probe pulses. The beam path inside the monochromator is shown in Fig. 5.2 **(b)**. For detection wavelengths 650 nm and 700 nm, a 800 nm interference filter was used to decrease the intensity of probe pulse around the wavelength of the supercontinuum seed, i.e. 786 nm. For detection wavelengths above 700 nm, a high-pass filter with cut-off wavelength at 850 nm was used instead of the interference filter. This was to avoid pollution from light with wavelengths equal to half of the wavelength the monochromator was set to select. The narrow band of the probe pulses selected out by the monochromator is finally detected by a photodiode detector. A Thorlabs Silicium photodiode (PDA36A-EC) is used to measure the intensity of the spectral increment selected by the monochromator in the visible. In the infrared, a Thorlabs InGaAs photodiode (PDA10CF-EC) is used. Relevant specifications for each photodiode is presented in the Table 5.1

Type	Wavelength range	Rise time	Active area
Si	200-1100 nm	Gain dependent	13 mm^2
InGaAs	800-1700 nm	2.3 ns	0.2 mm^2

Table 5.1: Specifications for the photodiode detectors used in the experimental setup.

Since the voltage over the photodiode detector (PhD) is proportional to the intensity of the light incident on it, I_0, absorbance change can be computed as

$$\Delta A = \log_{10}\left(\frac{I_0}{I_\text{p}}\right) - \log_{10}\left(\frac{I_0}{I_\text{np}}\right) = \log_{10}\left(\frac{V_\text{np}}{V_\text{p}}\right) \tag{5.1}$$

Where I_p and I_np are the light transmitted through the sample respectively with and without pumping, and V_p and V_np are the associated voltages registered by the PhD. A spinning chopper wheel was placed in the beam path of the pump. By knowing when the pump was blocked and unblocked respectively, V_{np} and V_p would be possible to read of from the photodiode detector. However, the chopper wheel were not synchronized with the voltage readings and only $|\Delta A|$ were obtainable without subjective analysis. The minimum and maximum voltage were registered for each reading of 2000 counts made by the PhD.

In order to control the time delay between the interaction of the pump pulse with the sample and the probe pulse with the sample, a delay-stage is incorporated in the beam path of the Integra-C pulses before they reach the sapphire crystal. The delay-stage has the capability of translating the retroreflector mounted on it by 1 m and is controlled by a step-motor. Moving the delay stage one step amounts to changing the time of arrival of the probe pulse at the sample by $t_\text{step} = 0.049$ ps.

As seen in Fig. 5.1, pump and probe pulses are focused onto the thin film sample by plano-convex lenses. The focus of the probe pulse is right at the sample, while the pump pulse is out of focus by 20 cm. In order to ensure that the part of the sample traversed by the probe pulse i uniformly excited, the radius of pump beam needs to be larger than the radius of the probe beam in the sample. Therefore, L_1 has significantly longer focal length than L_2 The focal length of L_1 is $f_1 = 1$ m and the focal length of L_2 is $f_2 = 0.2$ m. For a diffraction-limited focus, the radius of the central circle of the Airy disk, ρ, is

$$\rho = \frac{0.61\lambda}{NA} \tag{5.2}$$

Here NA, the numerical aperture of the lens, is equal to $n\sin(\theta_\text{max})$ where θ_max is the maximum half-angle of which light leaves the lens. By inserting $n = n_\text{air} = 1$ in Eq. 5.2 and using a 7 mm radius of the probe beam cross section before the lense[32], the area of the focused probe beam is $4.0 \cdot 10^{-4}$ mm^2 for $\lambda = 650$ nm and $1.4 \cdot 10^{-3}$ for $\lambda = 1200$ nm. The radius of collimated TOPAS output is not known, but a qualified guess is 5 mm. This gives an area of the focused pump beam of $1.3 \cdot 10^{-2}$ mm^2 for $\lambda = 520$ nm. A value for the pump cross-section area 20 cm away from focus can be found by using the following relationship for Gaussian beams

$$w(z) = w_0 \sqrt{1 + \frac{z}{\pi w_0^2/\lambda}}$$

where w is the radius of the beam at distance z from the focus and w_0 is the radius of the beam at the focus. One then finds that the area of the pump beam cross-section at the position of the sample is 0.9 mm^2.

As will be explained in the following section, 650 nm and 1200 nm are the smallest and largest wavelengths for which the transient absorption kinetics have been measured, and 520 nm is center wavelength of the pump pulses used for the measurements. Since the angle of incidence of the pump and the probe is less than 0.1°, the area of the spot size projected onto the sample is identical with the areas computed above. Therefore, this estimate yields that the area excited by the pump pulses is larger than the probed area by a factor of 10^2 for 1200 nm probe-light and by a factor of 10^3 for 650 nm probe light.

5.1.1 Characterisation of Supercontinuum pulses

Since the wavelengths at which it is possible to measure transient absorption kinetics is limited by the spectral width of supercontinuum (SC) pulses generated in the sapphire window, the spectral width of the SC pulses generated under the conditions used for the measurements presented in Ch. 6, is presented here.

The variables affecting the spectral width and stability of SC pulses are: The numerical aperture and intensity of the pulses incident on the sapphire window and position of the focus with respect to the front of the window. The SCG is best if the focus of the incident pulses are very close to the front of the sapphire window. The numerical aperture generally have to be as large as possible in order to create a filament with high intensity light in it. However, if this intensity becomes too high, the filament breaks up into multiple smaller filaments. Even though a broader spectrum than the one shown here (see Fig. 5.4) can be produced under conditions of multiple filaments,it is very unstable.

The appearance of the SC beam as it is blocked by a white card can be used to distinguish between multiple and a single filament and to check the quality of a single filament. This was used to optimize the SCG. Fig. 5.3 (a) and (b) shows two examples of stable supercontinuum generation (SCG) while Fig 5.3 (c) shows an example of unstable SCG due to formation of multiple filaments. In fig. 5.3(c), the presence of multiple filaments is revealed by the bright and dark contrast in the central white disk. The bright section of this area is actually a collection of smaller bright dots which are not resolved in the picture, each of which is caused by an individual filament.

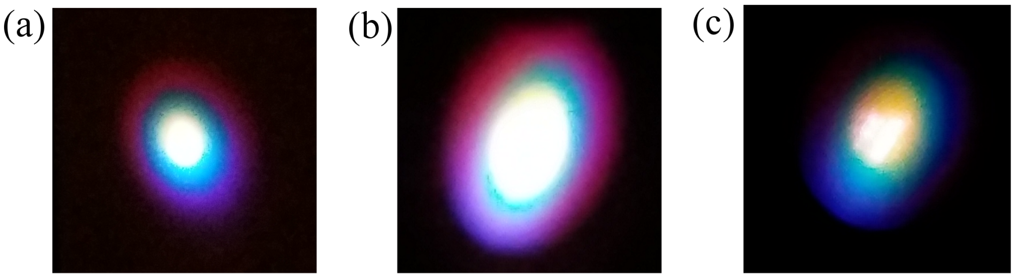

Figure 5.3: The transverse profile of the supercontinuum light. (a) and (b) is the profile of a single filament and (c) is the profile SCG in multiple filaments. Pictures were taken with a smart-phone camera.

The images presented in Fig. 5.3 (b) and (c) show increased astigmatism. This is because these pictures were taken after accidental misalignment of the beam path into the SCG-arrangement.

The spectrum of the SC pulses after passing through the 800 nm interference and 850 nm high pass filter respectively, was measured with an Avaspec fiber spectrometer. Due to the 1100 nm cut-off of the silicon CCD array in the spectrometer, wavelengths above this value could not be detected.

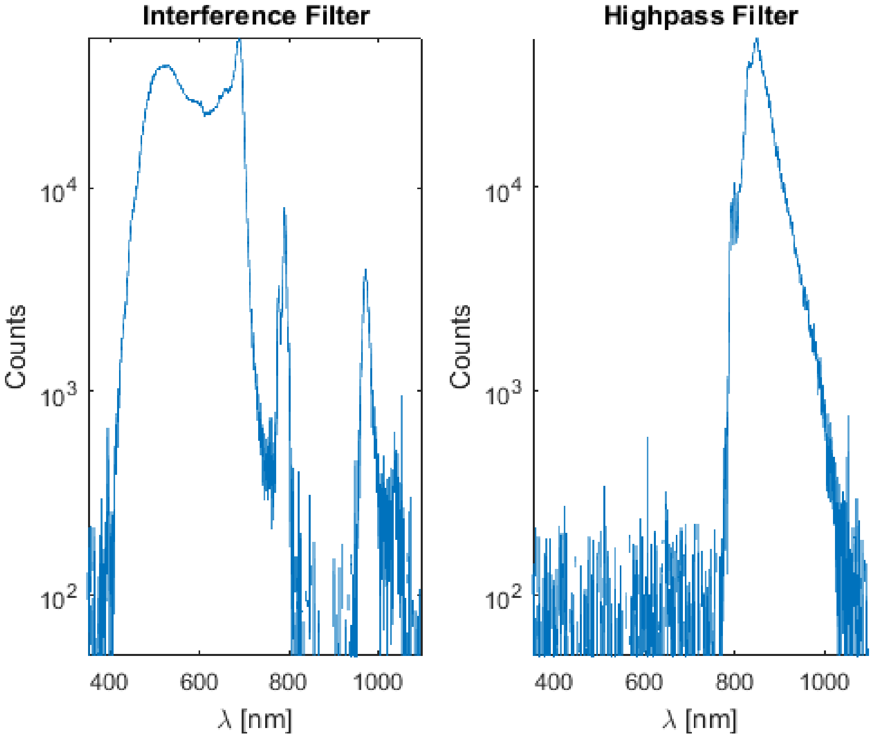

Figure 5.4: The visible and near infrared spectrum of the supercontinuum pulses with a 800 nm interference filter (left) and a high pass filter with 850 nm cut off (right) employed.

The spectrum was obatined for SCG where the image of a screen were similar to Fig. 5.3 **(a)** and **(b)**.

5.2 Transient Absorption Spectroscopy on P3HT:PCBM

This section outlines the possibilities of transient absorption spectroscopy on P3HT:PCBM solar cells and P3HT films, and what excited species there is to look for in the visible and near-infrared parts of the electromagnetic spectrum.

The wavelengths selected for the transient absorption kinetics measurements presented in Ch. 6, has been chosen on the basis of the transient absorption spectra for P3HT and PCBM:P3HT reported in refs 34 and 22 respectively. An effort for finding publications contradicting these references have been made and none was found. The transient absorption spectrum of RR-P3HT a few picoseconds after excitation with a 400 nm pump has the following features: Decreased absorbance due to ground-state bleach at wavelengths where ground state absorption occurs, a narrow peak of increased absorbance at 650 nm attributed to electro-absorption of ground state molecules due to the electric field of positive and negative polarons bound in pairs and a broad peak of increased absorption entered at 1200 nm due to photoabsorption by singlet excitons. Ito and coworkers find that the peak at 650 nm is found to decay exponentially with a single lifetime of 0.8 ps (80%) and a constant fraction (20%). Here, the percentages in the brackets refer to the fraction of the constant factor in front of the exponential term out of the sun of the constant factors for all the terms in function. The broad exciton peak is, by Ito and coworkers, fitted to a sum of three exponential one of which is fixed to 330 ps, their measured value for the luminescence lifetime of the P3HT. The average of the two other lifetimes is intensity dependent starting at 26 ps (58 %) and ending at 24 ps (92 %) for pulse fluences of 1 and 24 $\mu J \cdot cm^{-2}$ respectively. After 3 ns, Ito and coworkers report a broad peak of increased absorbance with peak value at around 1000 nm. This is attributed to absorption due to the presence of polarons. As for polaron pairs, the effect increased absorbance at these wavelengths is caused by electro-absorption: The result of reduced band-gab, i.e. energy difference between the HOMO and the LUMO, due to the deformation of the molecule. At low excitation fluence (1 $\mu J \cdot cm^{-2}$) the absorbance difference at 1000 nm remains constant over 3 ns, while a fraction of the polarons has decayed after 3 ns with excitation fluence $120 \mu J \cdot cm^{-2}$.

For P3HT:PCBM blends, the same features as for P3HT was observed immediately after excitation, but the long lived polaron band broadens to a single band reaching from 700 nm to 1000 nm with approximately equal magnitude of absorbance change over the range. The band was detectable on the ms time scale. They conclude that the band is due to polarons in different circumstances. Based on a microsecond transient absorption study[35] the transient absorption around 700 nm and 1000 nm is due due to interchain delocalised polarons in crystalline P3HT aggregates and localised intrachain polarons in disordered

P3HT-domains. Here, the latter type of domains domains would be interfacial volume between crystalline P3HT domain and aggregates of PCBM nanocrystals. Additionally, the the transient absorption at around 850 nm is deduced to primarily be caused by localised polarons bound PCBM anions in the disordered domains between the P3HT crystalline regions and PCBM nanocrystal aggregates. The absorbance change at 850 nm was found to decay monoexponentially with a $\sim$ 500 ps lifetime, while at 700 and 1000 nm the absorbance change was constant on the ns time scale and could even be observed after milliseconds.[22]

Due to the above mentioned points, the transient absorption kinetics were measured at 650 nm, 700 nm, 1000 nm and 1200 nm in order to see if the results could be reproduced and eventually to use some of the data to deduce the efficiency of charge separation and thickness of the P3HT domains. The measurements were done with a excitation wavelength of 520 nm. This is because the P3HT has maximum absorbance at around this wavelength [28]

The measurements presented in this project, were done with a 4 mW pump pulse train incident on the samples. By using the area of the pump spot size estimated in Sec. 5.1, an estimate for the pulses as they interact the samples is 444 $\mu J \cdot cm^{-2}$. This means the bimolecular recombination of both excitons and polarons play a dominating role for the measurements presented here. For study of exciton diffusion and charge separation in BHJ solar cells, exciton-exciton annihilation needs to be negligible as a decay channel. This is not the case for 444 $\mu J \cdot cm^{-2}$ excitation. Rather, it is expected to be completely dominating for the exciton decay. The 700 nm and 1000 nm polarons should also recombine bimolecularly[35] , but slower than the excitons.

Chapter 6

Measurements of Transient Absorption Decay in P3HT and P3HT:PCBM

This chapter presents the measurements of transient absorption (TA) kinetics of P3HT and P3HT:PCBM made with the experimental set-up described in Sec. 5.1. This is done for the selected wavelengths: 650 nm, 700 nm, 850 nm, 1000 nm, 1100 nm and 1200 nm.

Three thin-film samples made by spin-coating on ITO-covered BK7 substrates have been investigated[1]. The layers for the three samples are

- "P3HT": BK7/ITO/ZnO/P3HT
- "P3HT:PCBM-a": BK7/ITO/ZnO/P3HT:PCBM
- "P3HT:PCBM-b": BK7/ITO/ZnO/P3HT:PCBM

The ZnO films were made by spin-coating and then annealing for 15 min at 130 $°C$. The P3HT-layer was made by spincoating P3HT dissolved in chlorobenzene onto the ZnO-layer and then annealing it for 10 min at 145 °C. For P3HT:PCBM-a and -b, P3HT and PCBM dissolved in chlorobenzene in weight ratio 1:1 was spin-coated onto the ZnO layer. For either P3HT:PCBM-a or P3HT:PCBM-b, the P3HT:PCBM layer was annealed for 10 min at 145 °C.

6.1 Permanent Bleaching of the Samples

In this section, "Sample 1" refers to the "P3HT", "sample 2" refers to "P3HT:PCBM-a" and "sample 3" refers to "P3HT:PCBM-b". The first attempts of data acquisition from

---

[1] The samples were handed to the author from the Mads Clausen Institute at SDU.

sample 1 were unsuccessful due to permanent bleaching of the P3HT film upon exposure to the pump beam. This was immediately observable due to increased transparency in the area exposed to the pump beam, see Fig. 6.1

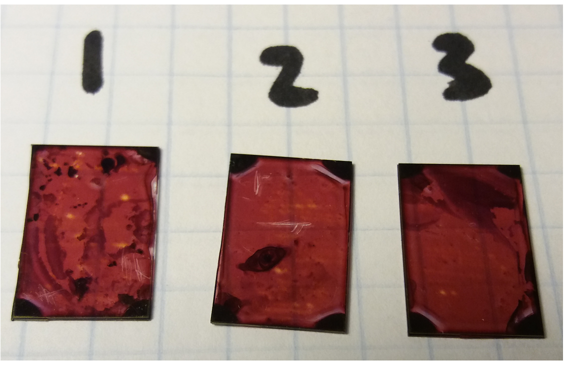

Figure 6.1: The samples after the course of all measurements. Bleaching is apparent in spots exposed by the pump.

The rate of bleaching was assessed by repeatedly measuring the transient absorption signal at time-zero for a duration of several minutes. The results are shown in Fig. 6.2 below

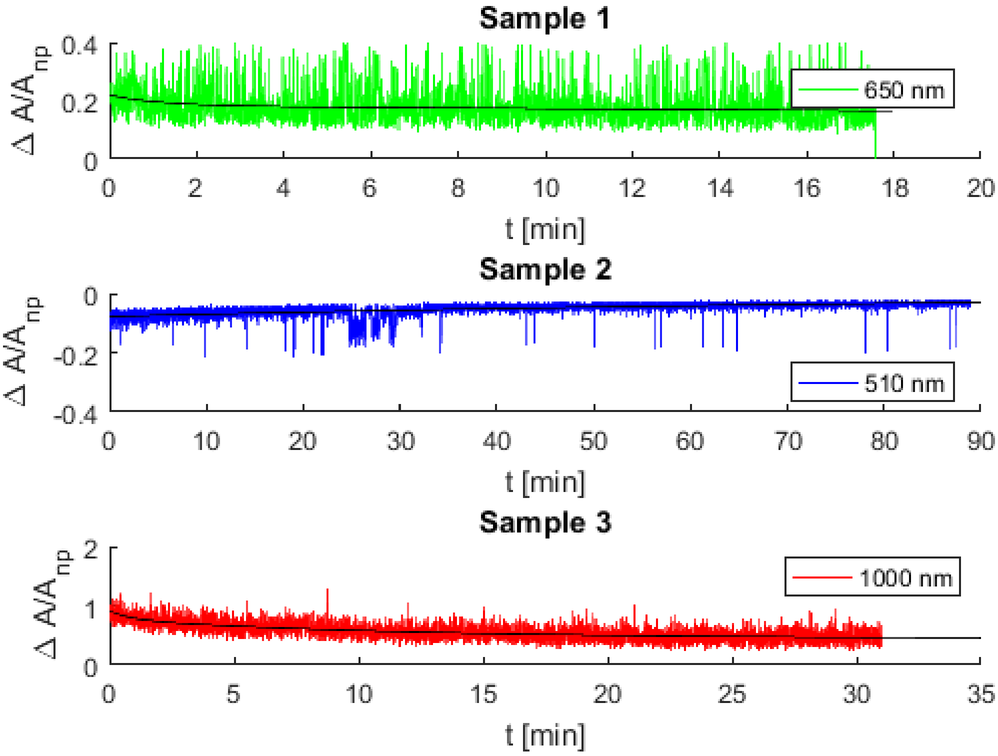

Figure 6.2: Permanent bleaching of the samples. The black lines are biexponential fits.

The Fitting parameters achieved by fitting the permanent bleaching data to a biexponential function of the form $a_1 \cdot e^{-t/\tau_1} + a_2 \cdot e^{-t/\tau_2} + k$, gives

Sample	$\underline{\tau_1}$ [min] ; a_1	$\underline{\tau_2}$ [min] ; a_2	k
1	$\underline{1.13}$; 0.037	$\underline{100}$; 0.11	0.074
2	$\underline{\tau_1}$; 0	$\underline{96.2}$; -0.078	0
3	$\underline{0.79}$; 0.13	$\underline{11.7}$; 0.33	0.44

Table 6.1: Fitting parameters for the data presented in Fig. 6.2.

The decrease in absorbance change after 15 min were as follows: 24.5% in sample 1, 14.5 % in sample 2 and 81.65% in sample 3.

The large discrepancy in rate of permanent bleaching should not be due to the fact that the traces have been measured at different wavelengths. If no excited states survives the duration between consecutive pump pulses, as the increase of the permanent bleaching is probably due to destruction of molecules and therefore not tied up on excited species.

An attempt to avoid bleaching was made by reducing the intensity of the pump beam. This was unsuccessful probably due to too low signal-noise ratio. Instead, the problem was helped by mounting the samples on a translation stage and manually moving the sample after each scan.

I took 1.11 minutes to do one scan with 20 step intervals and half of that to do one scan with 40 step intervals.

6.2 Transient Absorption Decay in P3HT

With the purpose of analysing the decay dynamics of singlet excitons and polarons in annealed P3HT, the transient absorption measured while the delay time was scanned from ∼ 20ps before time zero to ∼ 570ps after time-zero with either 1 ps or 2 ps intervals. Due to a high amplitude of noise relative to the amplitude of the signal, samples of 10 consecutive scans were recorded for each of the selected wavelengths. The average of each set of 10 scans were then computed.

The measurements at 1200 nm sample were heavily influenced by a large signal-to-noise ratio due to low spectral energy density of the probe pulses at this wavelength (See Fig. 5.4). This was why the measurements with 1100 nm detection wavelength were made for study of the exciton decay. The tail of the polaron transient absorption should still be influential at 1100 m, so the transient absorption decay is not absolutely due do excitons[22].

At the wavelengths considered, deviations from the ground-state absorption of the samples is expected to positive on the picosecond time scale, as argued in Sec. 5.2. This means that the maximum voltage was assigned to V_{np} and the minimum voltage to V_{p}. It should be noted that large spikes occurring at seemingly random times in the data has been excluded from the dataset, as described in App. B.

The average of the change in absorption normalised to the absorbance without pumping, A_{np}, is shown in Fig. 6.3 on the following page. A_{np} for each sample was measured by reading from a Hewlett Packard multimeter , which displaying the voltage over the photodiode. The average of ten pairs of voltage-readings for each sample for each wavelength done with the longest possible integration time of 100 power line cycles yielded the following ground-state absorbances shown in Table 6.2.

A_{np}	650 nm	700 nm	850 nm	1000 nm	1100 nm	1200 nm
P3HT	0.25	0.16	0.070	0.065	0.11	0.10
P3HT:PCBM-a	0.12	0.13	0.054	0.051	0.12	0.022
P3HT:PCBM-b	0.22	0.14	0.10	0.057	0.13	0.093

Table 6.2: Ground state Absorbance

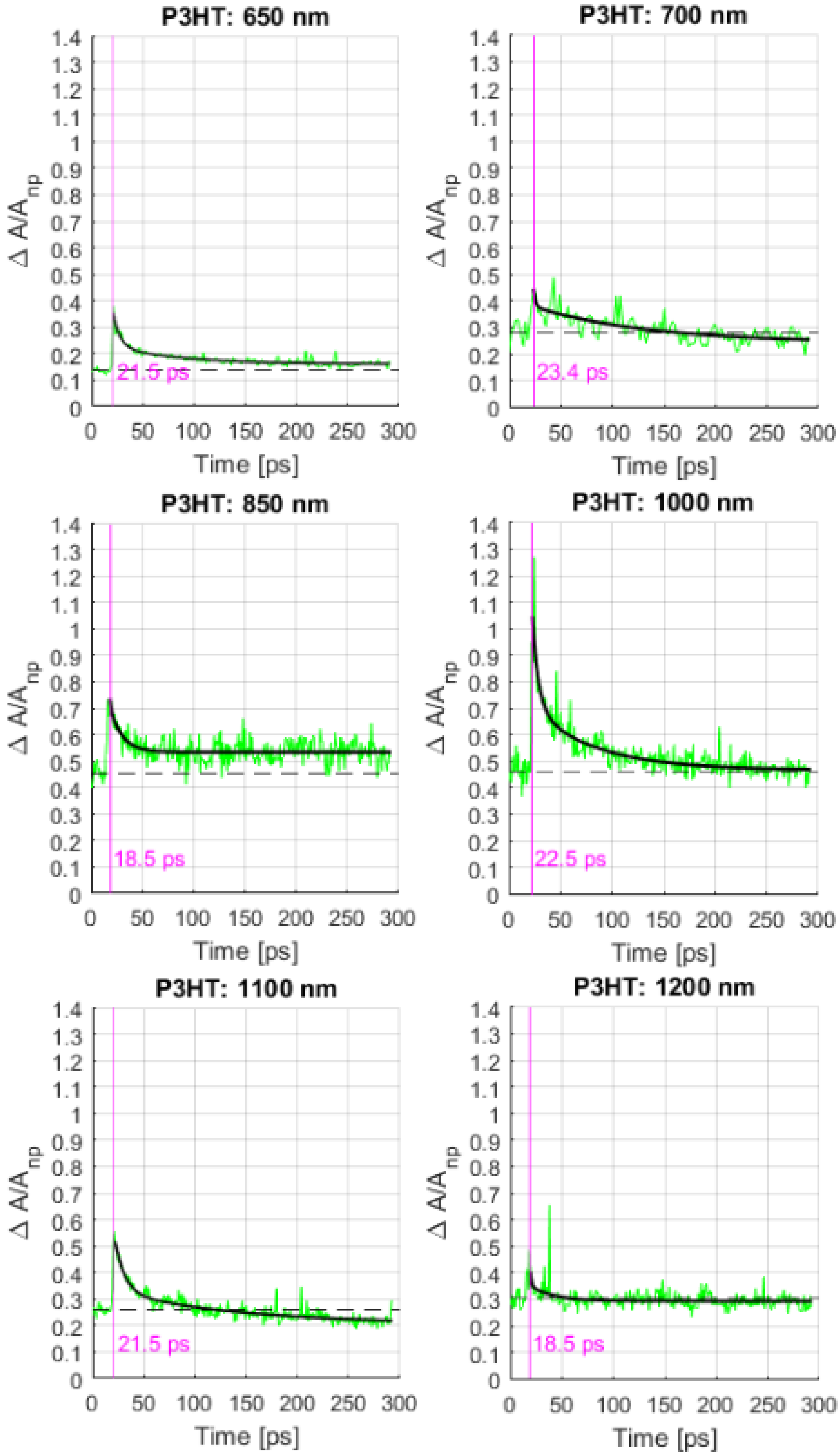

Figure 6.3: Transient absorption traces in P3HT at selected wavelengths. Time zero is marked in magenta, and the average $\Delta A/A_{np}$ without signal is marked in dotted black.

The traces, overall, have a sharp rise in signal followed by a decay. This is with exception for the 700 and 1200 nm datasets. The plot of the data for the 700 nm shows worse signal-noise ratio than the other ones. For 1200 nm, a short large rise in signal at around 40 ps exceeds the signal at the apparent time zero by a factor of 1.6, which is attributed to noise.

All the datasets have a nonzero $\Delta A/A_{\text{np}}$ before time-zero. The average value of $\Delta A/A_{\text{np}}$ without signal has been estimated by computing the average of the $\Delta A/A_{\text{np}}$ -values measured from 0 ps to 10 ps before time zero. This value will be referred to as k_0 and its values for the different datasets can be found in Table 6.3. The nonzero k_0 can be caused by two things. For the first part, noise produces a constant and nonzero $\Delta V = V_{\text{max}} - V_{\text{min}}$ when averaging over 10 scans. For the second part, excited states reminiscent from the previous excitation will contribute to an absorbance change prior to time zero. In pure P3HT this is likely not the case as a possibility since the longest lived excited species, namely polarons, has been reported to disappear on the nanosecond time scale[34] and there is one millisecond between each pump pulse in this set-up.

Another remark to be made about the data presented in Fig. 6.3 is the large magnitudes of $\Delta A/A_{\text{np}}$. The variations in $\Delta A/A_{\text{np}}$ are larger by a factor of 100 compared to the values found in TAS studies. This is due to the relatively high pulse-fluence. In fact, for the 444µJ pump-pulse fluence used in this experiment, the excitons are expected to decay via exciton-exciton annihilation on the picosecond time scale. This is based on ref. 28, where 500 nm pump pulses with fluencies of a quarter of a 250µJ proved to provide a concentration of excitons in pristine P3HT:PCBM which was high enough to decay via exciton-exciton annihilation with a lifetime of a few picoseconds. Furthermore, the decay of polarons i the P3HT film is also expected to be dominated by polaron-polaron annihilation but with a slower lifetime than excitons[36]. In order to quantitatively analyse the decays, the averaged datasets for P3HT presented in Fig. 6.3 have been fitted to biexponential functions of the form

$$\Delta A/A_{\text{np}}(t) = a_1 \cdot e^{-(t-t_0)/\tau_1} + a_2 \cdot e^{-(t-t_0)/\tau_2} + k \tag{6.1}$$

The values for the parameters of Eq. 6.1, with exception of t_0, are summarised in Table 6.3. t_0 was fixed to the time corresponding to the first datapoint after the point of maximum $\Delta A/A_{\text{np}}$. This is with exception for the measurement at 700 nm where the second highest value of $\Delta A/A_{\text{np}}$ was judged to be the point of timely overlap. It should be noted at only the data points for which the delay time was equal to t_0 or higher were included in the fits.

λ_{probe}	Material	$\underline{\tau_1}$[ps] ; a_1[%]	$\underline{\tau_2}$[ps] ; a_2[%]	$k - k_0$[%]	k	k_0
650 nm	P3HT	$\underline{6.2}$; 51	$\underline{64.3}$; 35	14	0.16	0.13
	P3HT:PCBM-a	$\underline{14.1}$; 49	$\underline{243}$; 51	0	0.26	0.33
	P3HT:PCBM-b	$\underline{5.0}$; 35	$\underline{94.2}$; 53	12	0.17	0.15
700 nm	P3HT	$\underline{1.9}$; 15	$\underline{112}$; 85	0	0.24	0.28
	P3HT:PCBM-a	$\underline{4.1}$; 22	$\underline{595}$; 78	0	0	0.33
	P3HT:PCBM-b	$\underline{0.87}$; 7	$\underline{42.6}$; 59	34	0.29	0.24
850 nm	P3HT	$\underline{1.2}$; 5	$\underline{11.5}$; 64	31	0.53	0.45
	P3HT:PCBM-a	$\underline{8.8}$; 57	$\underline{187}$; 37	6	0.61	0.57
	P3HT:PCBM-b	$\underline{0.8}$; 16	$\underline{19.4}$; 48	35	0.37	0.28
1000 nm	P3HT	$\underline{6.3}$; 56	$\underline{62.9}$; 43	1	0.47	0.46
	P3HT:PCBM-a	$\underline{5.4}$; 48	$\underline{127}$; 52	0	0.53	0.56
	P3HT:PCBM-b	$\underline{2.57}$; 44	$\underline{43.9}$; 55	1	0.46	0.45
1100 nm	P3HT	$\underline{9.4}$; 61	$\underline{120}$; 39	0	0.21	0.26
	P3HT:PCBM-a	$\underline{6.19}$; 66	$\underline{62.6}$; 34	0	0.2	0.22
	P3HT:PCBM-b	$\underline{1.3}$; 29	$\underline{23.5}$; 71	0	0.19	0.20
1200 nm	P3HT	$\underline{1.0}$; 49	$\underline{22.7}$; 51	0	0.29	0.30
	P3HT:PCBM-a	$\underline{1.2}$; 59	$\underline{40.9}$; 35	6	1.4	1.36
	P3HT:PCBM-b	$\underline{7.7}$; 100	-	0	0.33	0.33

Table 6.3: Parameters found by fitting the transient absorption data for P3HT, P3HT:PCBM-a and P3HT:PCBM-b to Eq. 6.1.

Since k_0 is attributed to noise, it can be subtracted from k in order to obtain a more correct value for the constant term in the $\Delta A/A_{\text{np}}$-signal. $(k - k_0)/[a_1 + a_2 + (k - k_0)]$ therefore gives a good estimate of the relative size of the constant part of the signal. Values for this quantity is therefore included in Table 6.3. The datasets for 700 nm and 1100 nm of P3HT has a crossing of the signal beneath the magnitude of absorbance change before time-zero. This is assumed to be due a poor correspondence between k_0 and the no-signal $\Delta A/A_{\text{np}}$ averaged over a larger sample size. In the cases where $k_0 > k$, $k - k_0$ has been set to zero in Table 6.3.

Looking at the plots of Fig. 6.3 and the fitting parameters for the datasets they present, gives information about the excited states which can partly be explained. The 650 nm trace should capture the dynamics of polaron pairs. As mentioned in Sec. 5.2, polaron pairs have been reported to partly decay with a lifetime $\sim$ 0.8 ps (80%) and remain constant ($\sim$20 %) in P3HT[34]. The fast decay was here determined to happen monomolecularly, since the lifetime was independent of excitation intensity in the range $15 - 120\mu\text{J} \cdot \text{cm}^{-2}$. While the constant fraction measured here is in good agreement with ref. [34], the average exponential decay at 650 nm, $(\tau_1 + \tau_2)/2 = 35.5$ ps [2] means either that the polaron pairs live longer in the P3HT film studied here, or that something else is causing the transient absorption. At 700 nm there is a large long lived fraction of lifetime 112 ps (85%), which be due to bimolecular decay of polarons in the crystalline domains of the annealed P3HT. The appearance of the fast decay, 1.9ps(15 %), is maybe due to the high-energy tail of the singlet exciton absorption. The 850 nm trace has a constant fraction of 31 % which could be due to long-lived polarons not recombining bimolecularly. However, this is not obvious since the mobility of polarons should be high in the annealed P3HT. The short lived fraction of the 850 nm decay is probably due to singlet excitons recombining bimolecularly. The lifetime of 11.5ps (56 %) is similar to the shortest lifetimes resulting from the 1000 and 1100 nm fits, where singlet excitons also should contribute to the transient absorption. The long lived decay at 1000 nm of 62ps(43%) could be due to polarons recombining bimolecularly, however, this is not obvious since the long lifetime at 1100 nm is 120 ps (39 %).

This decay could also be due to a fraction of excitons not annihilated with other excitons decaying radiatively, either way, the decay at 1100 nm should be the same as the decay at 1000 nm.

The 1200 nm trace has an average lifetime of longest lifetime of 11.9 ps and no constant fraction. This fits nicely with the fact that polarons do not contribute to the absorbance change at this wavelength.

6.3 P3HT:PCBM

As for the measurements of the transient absorption of P3HT, the data for the P3HT:PCBM-samples is averages of 10 scans taken with filtration of large random spikes in the signal as described in App. B The result of the measurements for P3HT:PCBM-a and -b is presented in Fig. 6.4 and 6.5 on the following pages. The result of biexponential fits to these datasets are summarised together with the parameters for P3HT in Table 6.3 in Sec. 6.2. For these measurements, it is not so clear if the nonzero $\Delta A/A_{np}$ might be due to long lived polarons. As mentioned in Sec. 5.2, the polarons in P3HT can be observed even milliseconds after the excitation. However, the density left after the period of the pump pulses (1 millisecond) is here assumed to be sufficiently small to be noticeable on the picosecond time-scale compared to the high-fluence excitations used for these measurements.

For the P3HT:PCBM-a 650 nm trace, time zero varied for each individual of the 10 scans due to imperfect function of the step-motor controlling the delay stage. This has been compensated for as described in App.C. Furthermore, the first two datapoint of this trace has not been included in the computation of k_0 since, an extreme $\Delta A/A_{\mathrm{np}}$-value has its

---

[2] Fitting the 650 nm data to a monoexponential function gives a lifetime of 21.5 ps (43 %)

place at t=0. This is a spike due to just one of the 10 scans from which the shown average trace is computed, and is thus attributed to noise.

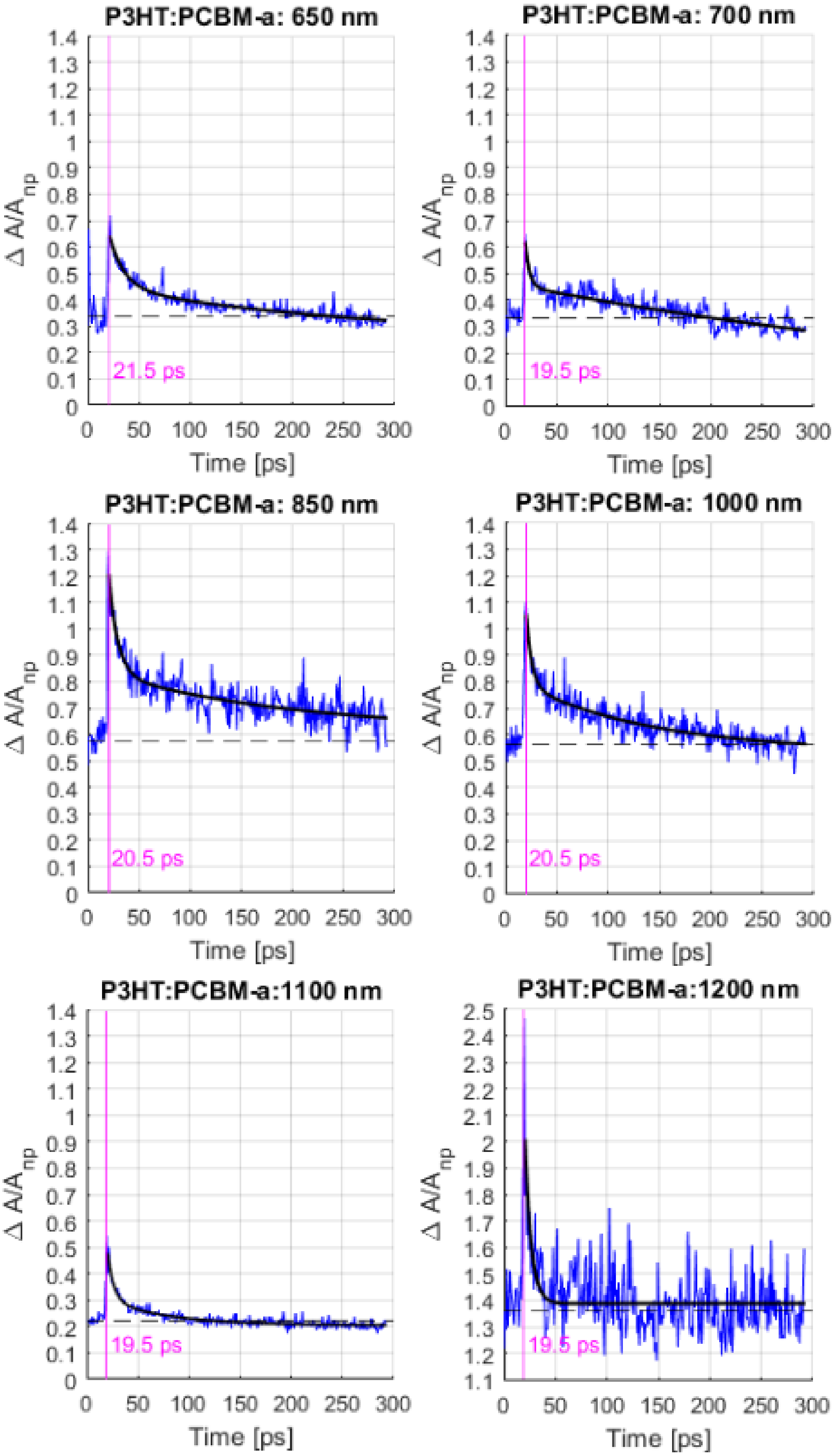

Figure 6.4: Kinetic traces of absorbance change in P3HT:PCBM-a at selected wavelengths. Time zero is marked in magenta, and the average $\Delta A/A_{np}$ without signal is marked in dotted black.

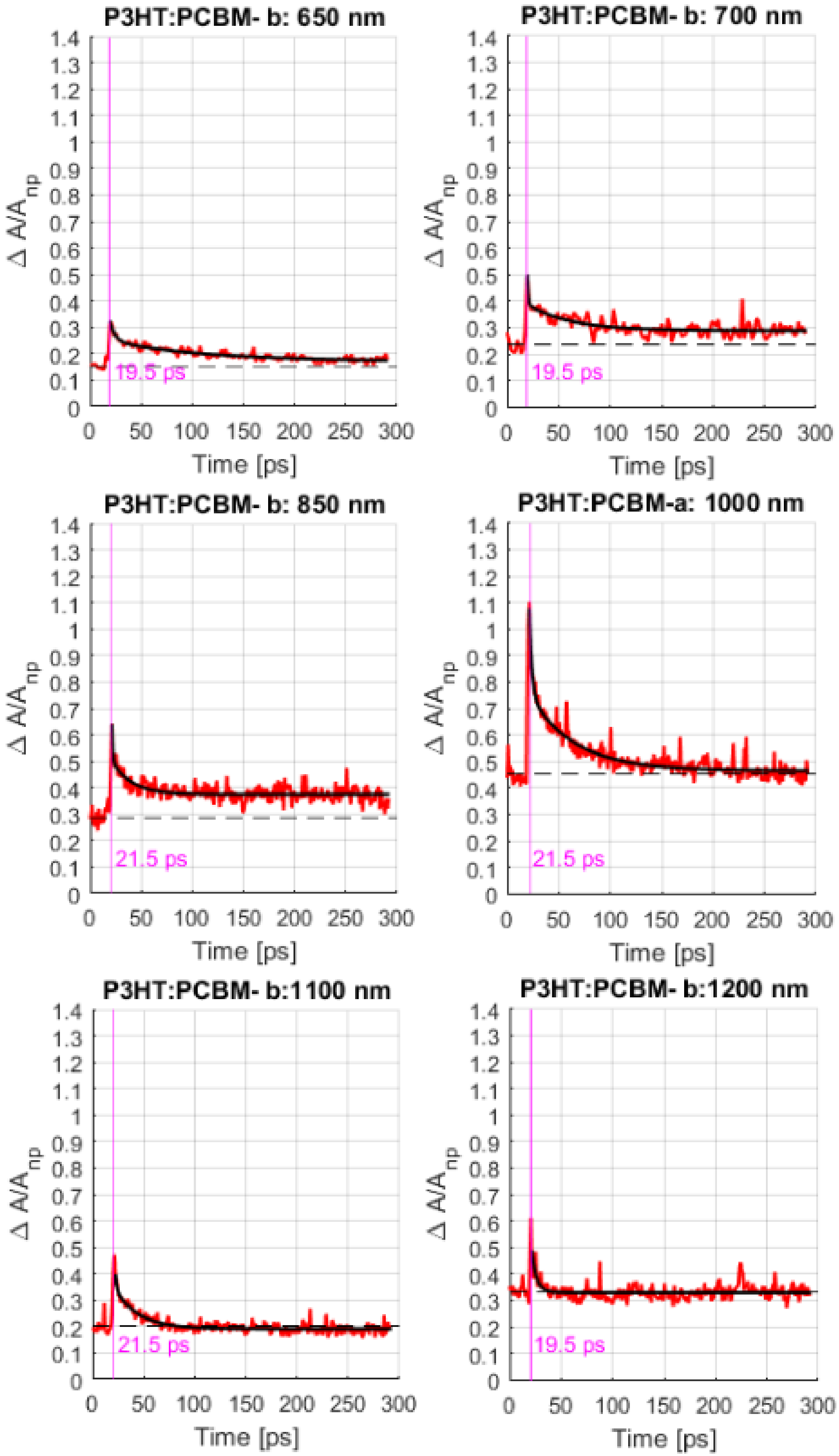

Figure 6.5: Kinetic traces of absorbance change in P3HT:PCBM-b at selected wavelengths. Time zero is marked in magenta, and the average $\Delta A/A_{\mathrm{np}}$ without signal is marked in dotted black.

A thing to note about the measurements of the P3HT:PCBM samples is that the longer τ_2 for 700 nm than for 1000 nm contradicts the theory of localised polarons in disordered domains causing transient absorption at 1000 nm and delocalised polarons in crystalline domains cause the the causes transient absorption at 700 nm. Furthermore, the day at 850 nm fall off relatively slow for both P3HT:PCBM-a and -b compared to the other wavelengths. This is consistent with the transient absorption at this wavelength as long delay times is due to P3HT polarons bound to PCBM anions. The increased localisation due to the coulomb binding, makes these polarons very unlikely to recombine bimolecularly. However, it is still much faster decays than what Ito and coworkers have measured ($\sim$ 500 ps).

In order to analyse the the charge separation process and exciton diffusion in P3HT:PCBM, the excitation fluence has to be lowered as to eliminate bimolecular recombination channels. However, bimolecular recombination could be studied in both P3HT and P3HT:PCBM instead via the obtained data of this project. In difussion-limited bimolecular recombination rate, $\gamma_b i$, is time dependent and given by the rate equation[35]:

$$\frac{\mathrm{d}n(t)}{\mathrm{d}t} = -\gamma_{bi}(t)n^2(t) \tag{6.2}$$

Here, $n(t)$ is the density of the excited species. Besides bimolecular recombination of individual excited species, exciton-polaron recombination should also be considered in order to give a complete picture.

Chapter 7

Conclusion

An transient absorption experiment has been build for investigation of excited state dynamics in P3HT and P3HT:PCBM in the visible and near-infrared. Transient absorption kinetics at selected wavelengths have been measured for an annealed P3HT- sample together with one annealed P3HT:PCBM-sample and one pristine P3HT:PCBM-sample. This involved broad-band probe pulses which were created by supercontinuum generation and consideration of the excited states in different nanometer-sized domains in P3HT:PCBM bulk heterojunctions.

The pump impacts the samples with pulse fluency of 444 µm. This implies densities of excited species so high that bimolecular recombination dominates over monomolecular decay processes, including exciton charge separation at the donor/acceptor interface. This is undesirable for studies of exciton diffusion and charge conversion efficiency in organic solar cells. In this regard, the project is inconclusive. Furthermore, the pump was found to permanently bleach the samples on a time scale of minutes, but with different rates. A P3HT:PCBM sample was found to be bleach significantly slower than the other P3HT:PCBM sample and the P3HT sample.

The lifetime of excited states in all of the samples had a significant short lifetime of 1 - 15 picoseconds and a longer lifetime ranging from 11-595 picoseconds. The magnitudes of the long lifetimes does not consistently describe polarons in accordance with the known transient absorption spectral features in mind. The short life times are within the expectations for decay through exciton-exciton annihilation.

Appendix A

Derivation of PDE for the complex pulse envelope

This derivation is after [29] The starting point is Maxwell's equations:

$$\nabla \times \vec{E}(\vec{r}, t) = \frac{\partial \vec{B}(\vec{r}, t)}{\partial t} \tag{A.1}$$

$$\nabla \times \vec{H}(\vec{r}, t) = \frac{\partial \vec{D}(\vec{r}, t)}{\partial t} + \vec{J}(\vec{r}, t) \tag{A.2}$$

$$\nabla \cdot \vec{D}(\vec{r}, t) = \rho(\vec{r}, t) \tag{A.3}$$

$$\nabla \cdot \vec{B}(\vec{r}, t) = 0 \tag{A.4}$$

and the constitutive relations

$$\vec{D}(\vec{r}, t) = \epsilon_0 \vec{E}(\vec{r}, t) + \vec{P}(\vec{r}, t) = \varepsilon \vec{E}(\vec{r}, t) \quad \text{and} \quad \vec{B}(\vec{r}, t) = \mu_0 \left(\vec{H}(\vec{r}, t) + \vec{M}(\vec{r}, t) \right) = \mu \vec{H}(\vec{r}, t)$$

By taking the curl of Equation 4.4 and eliminating the magnetic flux density, $\vec{B}$, via equation 4.5, one can obtain the wave equation

$$\nabla^2 \vec{E}(\vec{r}, t) - \frac{\partial^2 \vec{D}_L(\vec{r}, t)}{\partial t^2} = 2 n_0 n_2 \frac{\partial^2 \left(|\vec{E}|^2 \vec{E}(\vec{r}, t) \right)}{\partial t^2} \tag{A.5}$$

where $\vec{D}_L(\vec{r}, t)$ is the linear displacement vector. In obtaining Eq. A.5, the facts that $\nabla \times \left(\nabla \times \vec{E} \right) = \nabla \left(\nabla \cdot \vec{E} - \nabla^2 \vec{E} \right) \approx -\nabla^2 \vec{E}$ and the $(n_2)^2$ term is negligible has been used. Now, the electric field can be written as

$$\vec{E}(\vec{r}, t) = \Phi(x, y) E(\vec{z}, t) \tag{A.6}$$

where $\Phi(x, y)$ is the transverse distribution function. By substituting Eq. A.6 into the wave equation, averaging over the transverse coordinates and neglecting $\partial^2/\partial x^2$ and $\partial^2/\partial y^2$ terms, one obtains

$$\frac{\partial^2 \vec{E}(z,t)}{\partial z^2} - \frac{\partial^2 \vec{D}_L(z,t)}{\partial t^2} = 2n_0\bar{n}_2 \frac{\partial^2 \left(|\vec{E}(z,t)|^2 \vec{E}(z,t) \right)}{\partial t^2} \tag{A.7}$$

$\bar{n}_2$ is the effective nonlinear refractive index:

$$\bar{n}_2 = \frac{\int n_2 \Phi^2(x,y) dxdy}{\Phi^2(x,y)} \approx \frac{1}{2} n_2 \tag{A.8}$$

Assuming a plane wave, a linearly polarized electric field propagating in the z direction can be written as

$$\vec{E}(z,t) = A(z,t) e^{i(k_0 z - \omega_0 t)} \hat{e} \tag{A.9}$$

where $\hat{e}$ is a unit vector pointing in the direction of polarization of the electric field, ω_0 is the carrier frequency, k_0 is the wave number and $A(z,t)$ is the complex pulse envelope function. If the $(\omega_0 t - k_0 z)$ representation is used instead of $k_0 z - \omega_0 t$, sign changes will occur in the final reduced wave equation. Now, D_L can we written as the Fourier integral

$$\vec{D}_L(z,t) = \int_{-\infty}^{\infty} n_0^2(\omega) \underline{\vec{E}}(z,\omega) e^{-i\omega t} d\omega \tag{A.10}$$

where $\underline{\vec{E}}(z,\omega)$ is the Fourier transform of $\vec{E}(z,t)$:

$$\underline{\vec{E}}(z,\omega) = \frac{1}{2\pi} \int_{-\infty}^{\infty} \vec{E}(z,t) e^{i\omega t} dt \tag{A.11}$$

Hence, the linear polarization term on the left-hand side of the one-dimensional wave equation, Eq. A.7, is

$$\begin{aligned} -\frac{\partial^2 \vec{D}_L(z,t)}{\partial t^2} &= -\int_{-\infty}^{+\infty} -\omega^2 n_0^2(\omega) \underline{\vec{E}}(z,\omega) e^{-i\omega t} d\omega \\ &= \frac{c^2}{2\pi} \int_{-\infty}^{\infty} \int_{-\infty}^{\infty} k^2(\omega) A(z,t') e^{i\omega(t'-t)} e^{i(k_0 z - \omega_0 t')} \hat{e}\ d\omega dt' \end{aligned} \tag{A.12}$$

From here, the derivation of the reduced wave equation proceeds by substituting in the Taylor series expansion for $k^2(\omega)$ around ω_0:

$$k^2(\omega) = k_0^2 + 2k_0 k_0^{(1)}(\omega - \omega_0) + k_0 k_0^{(2)}(\omega - \omega_0)^2 + ... \tag{A.13}$$

where

$$k_0 = k(\omega_0) \qquad \text{and} \qquad k_0^{(n)} = \left. \frac{\partial^n k}{\partial \omega^n} \right|_{\omega=\omega_0}$$

k_0 is the propagation constant, $k_0^{(1)}$ is the inverse group velocity, and $k_0^{(2)}$ is the inverse group velocity of dispersion. By terminating the expansion for $k^2(\omega)$ after the second-order term,Equation A.12 simplifies to

$$\begin{aligned}-\frac{\partial^2 \vec{D}_L(z,t)}{\partial t^2} &= c^2 \int_{-\infty}^{\infty} \left[k_0^2 \delta(t'-t) + i2k_0k_0^{(1)}\delta^{(1)}(t'-t) - k_0k_0^{(2)}\delta^{(2)}(t'-t)\right] A(z,t') \\ &\quad \times e^{i(k_0z-\omega_0t)}\hat{e}\; dt' \\ &= c^2\left[k_0^2A(z,t) + 2ik_0k_0^{(1)}\frac{\partial A(z,t)}{\partial t} - k_0k_0^{(2)}\frac{\partial^2 A(z,t)}{\partial t^2}\right] e^{i(k_0z-\omega_0t)}\hat{e} \qquad \text{(A.14)}\end{aligned}$$

where $\delta^{(m)}(x)$ is the m'th order derivative of the Dirac-delta function, with the property that

$$\int_{-\infty}^{\infty} \delta^{(m)}(t-t_0)f(t)dt = \frac{\mathrm{d}^m f(t)}{\mathrm{d}t^n}$$

In writing Equation A.14, the following identities are helpful:

$$\begin{aligned}\frac{1}{2\pi}\int_{-\infty}^{\infty} e^{i(\omega-\omega_0)(t'-t)}d\omega &= \delta(t'-t) \\ \frac{1}{2\pi}\int_{-\infty}^{\infty} (\omega-\omega_0)e^{i(\omega-\omega_0)(t'-t)}d\omega &= i\delta^{(1)}(t'-t) \qquad \text{(A.15)} \\ \frac{1}{2\pi}\int_{-\infty}^{\infty} (\omega-\omega_0)^2e^{i(\omega-\omega_0)(t'-t)}d\omega &= -\delta^{(2)}(t'-t)\end{aligned}$$

Now, in the slowly-varying envelope regime, $|\partial^2 A(z,t)/\partial z^2)| \ll k_0|\partial A(z,t/\partial z)|$, so

$$\frac{\partial \vec{E}(z,t)}{\partial z^2} \approx \left[-k_0^2A(z,t) + 2ik_0\frac{\partial A(z,t)}{\partial z}\right] e^{i(k_0z-\omega_0t)}\hat{e} \qquad \text{(A.16)}$$

Im the same manner, the $\partial^2|A(z,t)|^2$ term on the right-hand side of Eq. A.7 is negligible for a slowly-varying envelope:

$$2n_0\bar{n}_2\frac{\partial^2\left(|\vec{E}(z,t)|^2\vec{E}(z,t)\right)}{\partial t^2} \approx -n_0n_2\omega_0^2|A(z,t)|^2Ae^{i(k_0z-\omega_0t)} \qquad \text{(A.17)}$$

Inserting the Equations A.14, **??** and A.17 into Equation A.7 gives

Appendix B

Filtration of Noise

Datapoints with differential absorption values larger than 0.4 were discarded an repeated. This was done to filter out single-pixel datapoints which occurred with seemingly random probability and with around the same magnitude (ΔA slightly larger than 0.4). 10 scans of sample at 1100 nm where the filter was not applied is shown below. For these ten scanes the average differential absorption values of the single-pixel spikes were 4.1 and had a variance of 0.0046. There were 95 of these spikes in the ten scans and six pairs of these happened at the same delay-time, namely at 289, 270, 251, 135, 108 and 89 ps. Overall, the spikes had seemingly random occurrence as can be seen in the figure below for sample 2 at 1100 nm.

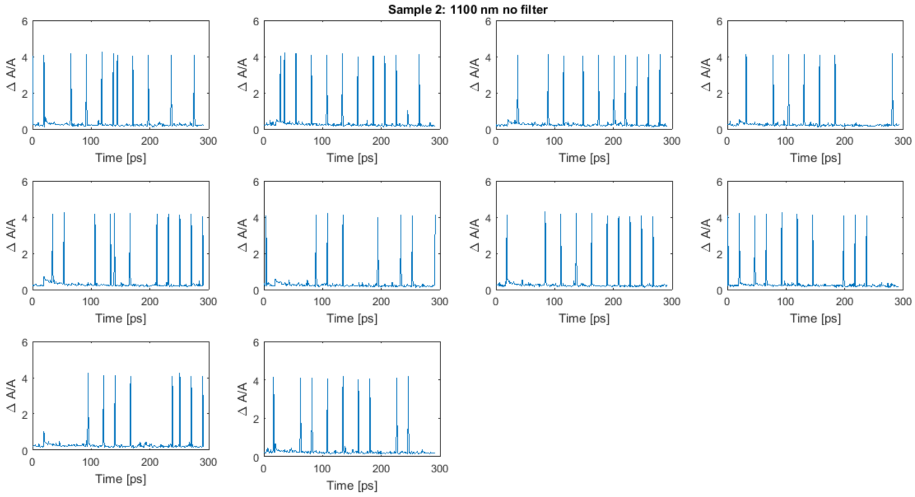

Figure B.1: Individual scans of sample 2 at 1100 nm without filtering of extreme values of differential absorption ($\Delta A/A > 3.48$).

The spikes we A sample of 10 individual scans and their average for sample 2 (P3HT:PCBM-a) at detection wavelength 1100 nm is shown below for comparison

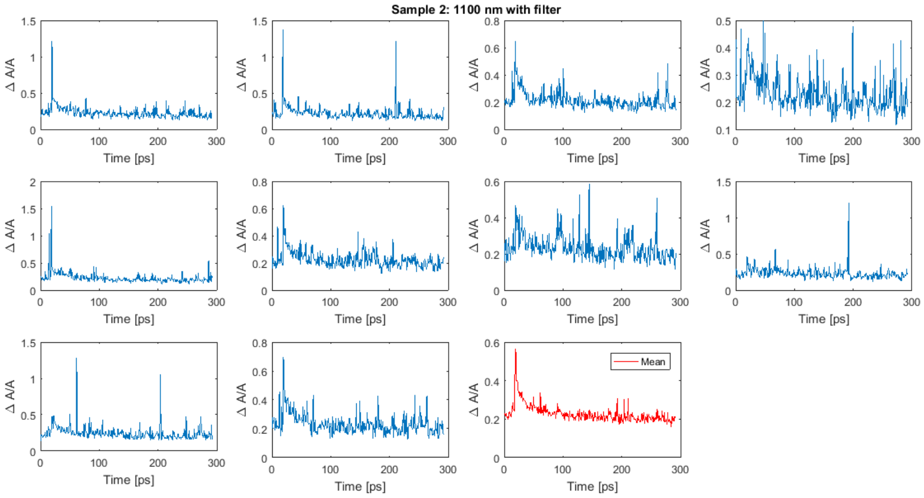

Figure B.2: Individual scans of sample 2 at 1100 nm with exclusion of datapoints where ($\Delta A/A > 3.48$)

Appendix C

Compensation for change in Time Zero

The scans for sample 2 (P3HT:PCBM-a) at $\lambda_{probe} = 650$ nm showed overlap at different points on the stage. This is likely due to errors of the stepping motor controlling the delay-stage. From each individual scan shown in Fig. C.1- C.4 below, it is seen that the point of maximum absorption appears to move backwards in time with increasing number of scans. The stepping motor was set to start at step 6000, corresponding to $t = 0ps$ on the plots, but it looks like it did not all the way back to that position for scans 4 to 10.

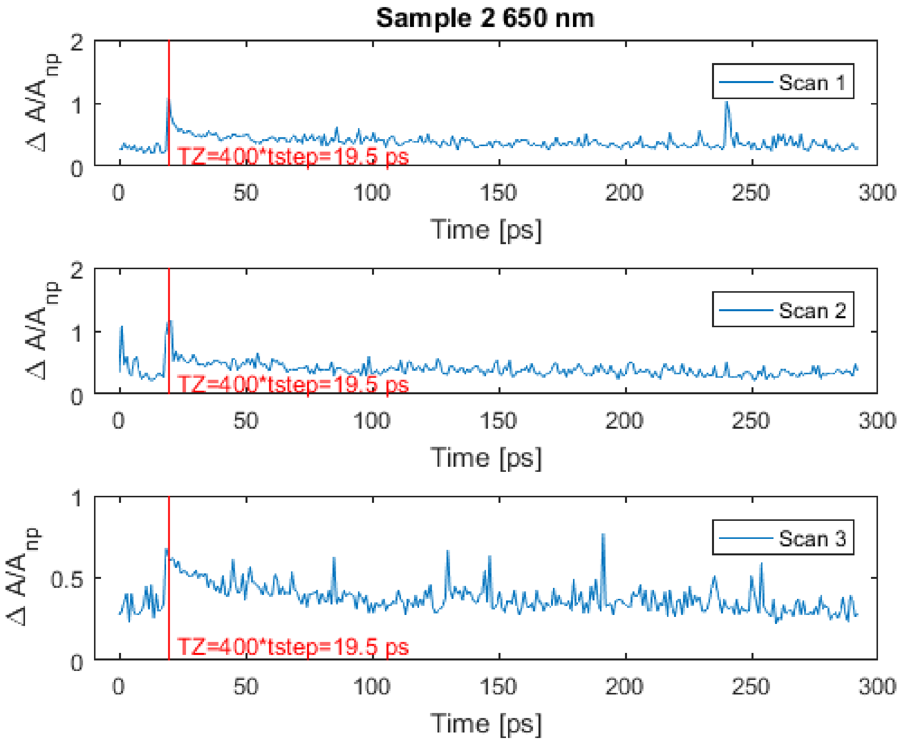

Figure C.1

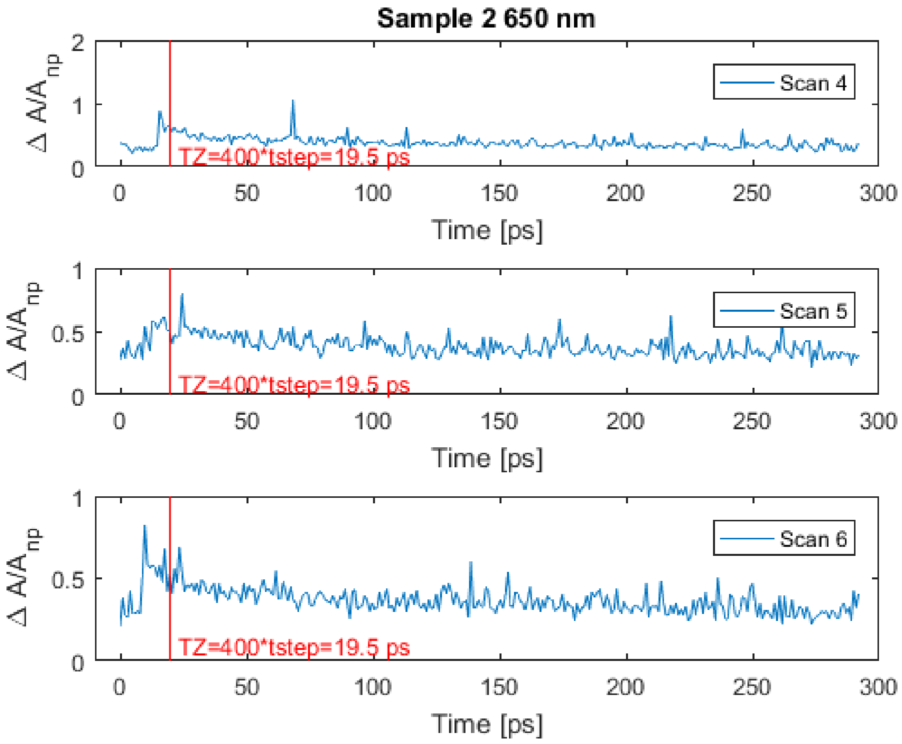

Figure C.2

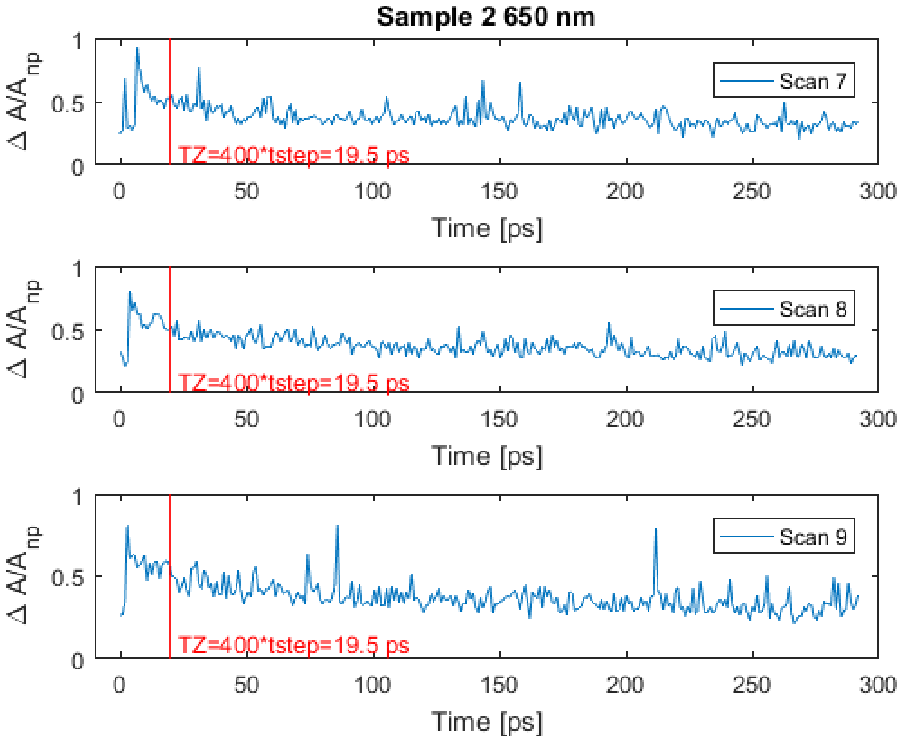

Figure C.3

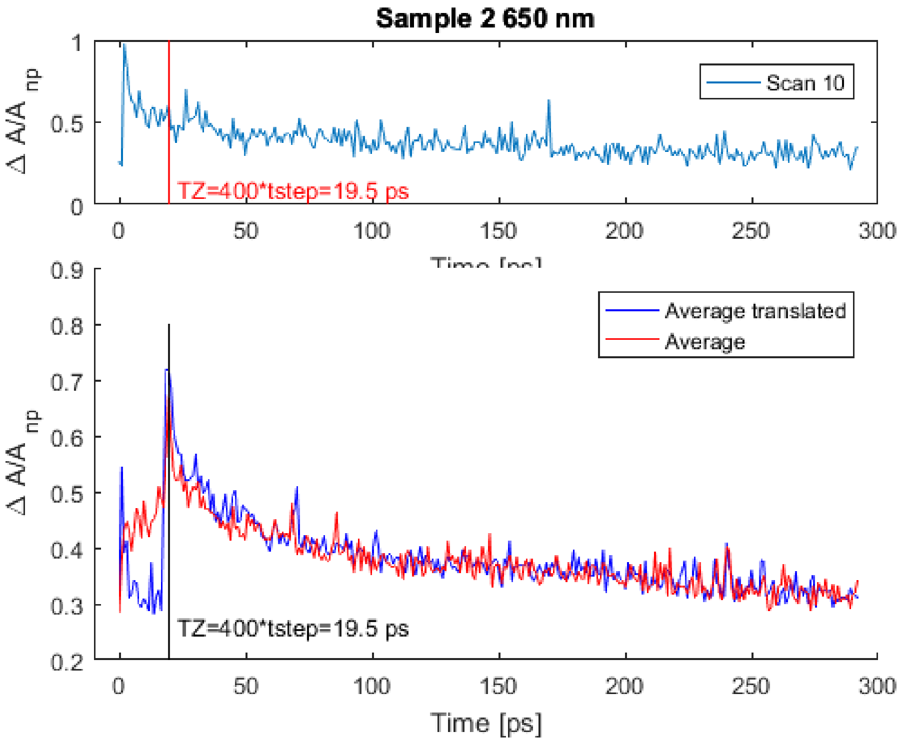

Figure C.4

The apparent change in time zero was compensated by translating the graphs in time such that the sudden rise followed by exponential decay, had its peak at 19.5 ps as is otherwise the case. For scan 5, the position where the probe and pump pulses have maximal overlap is not clear. Here the position for timely overlap was taken to be at the position where absorption difference rose from a level around 0.3 to a level around 0.5, even though it continued to increase for several picoseconds. Scan 2 also has a oeak right around $t = 0$ ps, which is regarded as noise because the exponential decay is quite clearly starting at 19.0 ps.

Bibliography

[1] Eds. K. Müllen, U. Scherf. Organic light emitting devices: Synthesis, properties and applications. 2006.

[2] Eds Z. Li, H. Meng. Organic light emitting devices: Synthesis, properties and applications. *Optical sceince and engineering series 111; CRC Press ; London: Boca Raton, FL.*, page 672, 2007.

[3] Benjamin Souharce Heiko Thiem Sybille Allard, Michael Foster and Ullrich Scherf. Organic semiconductors for solution-processable field-effect transistors (ofets). *Angewandte Chemie International Edition*, 47(22):4070–4098, 2008.

[4] Daniele Braga and Gilles Horowitz. High-performance organic field-effect transistors. *Advanced Materials*, 21(14-15):1473–1486, 2009.

[5] Harald Hoppe and Niyazi Sariciftci. Organic solar cells: An overview. *Journal of Materials Research*, 19(7):1924–1945, 2004.

[6] U. Scherf C. Brabec and Eds V. Dyakonov. Organic photovoltaics: Materials, device physics, and manufacturing technologies. *Wiley-VCH: Weinheim*, page 597, 2008.

[7] Suren A. Gevorgyan Thomas Tromholt Birgitta Andreasen Mikkel Jørgensen, Kion Norrman and Frederik C. Krebs.

[8] R. Rittberger F. Padinger and N. Sariciftci. Effects of postproduction treatment on plastic solar cells. *Advanced Funcitonal Materials*, 13(1):85–88, 2003.

[9] N. Sariciftci F. Padinger T. Fromherz S. Shaheen, C. Brabec and J. Hummelen. 2.5% efficient organic plastic solar cells. *Applied Physics Letters*, 78(6):841–843, 2001.

[10] J. Hummelen F. Wudl G. Yu, J. Gao and A. Heeger. Polymer photovoltaic cells - enhanced efficiencies via a network of internal donor-acceptor heterojunctions. *Science*, 270(5243):1789–1791, 1995.

[11] M Scharber G. Dennler and C. Brabec. Polymer-fullerene bulk-heterojunction solar cells. *Advanced Materials*, 21(13):1323–1338, 2009.

[12] X. Gong K.Lee A. Heeger W. Ma, C. Yang. Thermally stable, efficient polymer solar cells with nanoscale control of the interpenetrating network morphology. *Advanced Functional Materials*, 15(10):1617–1622, 2005.

[13] J. Huang Y. Yao T. Moriarty K. Emery G. Li, V. Shrotriya and Y. Yang. High-efficiency solution processable polymer photovoltaic cells by self-organization of polymer blends. *Nature Materials*, 4(11):864–868, 2005.

[14] M. Schwoerer and H.C. Wolf. Organic molecular solids. *Wiley-VCH Verlag, Weinheim*, 2007.

[15] Martin Pope and Charles E. Swenberg. Electronic properties in organic crystals and polymers, 2nd edition. *Oxford University Press, Oxford*, 1999.

[16] J. Pouget. The peierls instability and charge density wave in one-dimensional electronic conductors. *Comptes Rendus Physique*, 17(3-4):332–356, 2016.

[17] Heinz Bässler and Anna Köhler. Charge transport in organic semiconductors. *Springer-Verlag Berlin, Heidelberg*, 2011.

[18] Edited by J. Singh and R. Williams. Excitonic and photonic processes in materials. *Springer*, 2015.

[19] Geoffrety A. Chamberlain. Organic solar cells: a review. *Solar Cells*, 8.

[20] Dieter Wöhrle and Dieter Meissner. Organic solar cells. *Advanced Materials*, 3(3):129–138, 1991.

[21] P. Heremans V. I. Arkhipov and H. Bässler. Why is exciton dissociation so efficient at the interface between a conjugated polymer and an electron acceptor? *Applied Physics Letters*, 82(25):4605–4607, 2003.

[22] H. Benten J. Guo, H. Ohkita and S. Ito. Charge generation and recombination dynamics in poly(3-hexylthiophene)/fullerene blend films with different regioregularities and morphologies. *Journal of the American Chemical Society*, 132(17):6154–6164, 2010.

[23] R. McCullough. The chemistry of conducting polymers. *Advanced Materials*, 10(2):93–116, 1998.

[24] R. Friend M. Nielsen K. Bechgaard B. Langeveld-Voss A. Spiering R. Janssen E. Meijer P. Herwig H. Sirringhaus, P. Brown and D. Leeuw. Two-dimensional charge transport in self-organized, high-mobility conjugated polymers. *Nature*, 401.

[25] S. C. Veenstra W. J. H. Verhees M.M. Wienk J. M. Kroon M. A. J. Michels X. Yang, J. loos and R. A. J. Janssen. Nanoscale morphology of high-performance polymer solar cells. *Nano Letters*, 5(4):579–583, 2005.

[26] G. de With S. S. van Bavel, E. Sourty and J. Loss. Volume organization of polymer and hybrid solar cells as revealed by electron tomography. *Advanced Functional Materials*, 20(19):3217–3234, 2010.

[27] S. Cho J. Byun J. S. Moon, J. K. Lee and A. J. Heeger. “columnlike” structure of the cross-sectional morphology of bulk heterojunction materials. *Nano Letters*, 9(1):230–234, 2009.

[28] Sebastian Albert-Seifried R. Alex Marsh, Justin M. Hodgkiss and Richard H. Friend. Effect of annealing on p3ht:pcbm charge transfer and nanoscale morphology probed by ultrafast spectroscopy. *Nano Letters*, 10(3):923–930, 2010.

[29] R. Alfano.

[30] P. Baum M. Bradler and E. Riedle.

[31] R. Boyd.

[32] Quantronix. *Integra-C Series Ultrafast Regenerative/Multi-pass Ti:sapphire Amplifiers - Operator's Manual*, Revision G, February 2009.

[33] Tsunami. *Tsunami Mode-Locked Ti:sapphire Laser - User's Manual*, 1995.

[34] H. Benten J. Guo, H. Ohkita and S. Ito. Near-ir femtosecond transient absorption spectroscopy of ultrafast polaron and triplet exciton formation in polythiophene films with different regioregularities. *Journal of the American Chemical Society*, 131(46):16869–16880, 2009.

[35] S. Yokoya H. Benten J. Guo, H. Ohkita and S. Ito. Bimodal polarons and hole transport in poly(3-hexylthiophene):fullerene blend films. *Journal of the American Chemical Society*, 132(28):9631–9637, 2010.

[36] F. Jamieson T. Clarke and J. Durrant.